HHS Public Access

Author manuscript

Cell Rep. Author manuscript; available in PMC 2022 March 17.

Published in final edited form as:

Cell Rep. 2021 September 14; 36(11): 109703. doi:10.1016/j.celrep.2021.109703.

Definitive hematopoietic stem cells minimally contribute to embryonic hematopoiesis

Bianca A. Ulloa[1,2], **Samima S. Habbsa**[1,2,5], **Kathryn S. Potts**[1,2], **Alana Lewis**[1,2,6], **Mia McKinstry**[1,2,7], **Sara G. Payne**[1,2,8], **Julio C. Flores**[2], **Anastasia Nizhnik**[1,2], **Maria Feliz Norberto**[1,2], **Christian Mosimann**[4], **Teresa V. Bowman**[1,2,3,9,*]

[1]Albert Einstein College of Medicine, Department of Developmental and Molecular Biology, Bronx, NY, USA

[2]Albert Einstein College of Medicine, Gottesman Institute of Stem Cell Biology and Regenerative Medicine, Bronx, NY, USA

[3]Albert Einstein College of Medicine and Montefiore Medical Center, Department of Medicine (Oncology), Bronx, NY, USA

[4]Department of Pediatrics, Section of Developmental Biology, University of Colorado School of Medicine and Children's Hospital Colorado, Anschutz Medical Campus, Aurora, CO, USA

[5]Present address: Hofstra/Northwell, Manhasset, NY, USA

[6]Present address: Coney Island Hospital, Brooklyn, NY, USA

[7]Present address: University of Washington, Seattle, WA, USA

[8]Present address: Cell Biology, Duke University, Durham, NC, USA

[9]Lead contact

SUMMARY

Hematopoietic stem cells (HSCs) are rare cells that arise in the embryo and sustain adult hematopoiesis. Although the functional potential of nascent HSCs is detectable by transplantation, their native contribution during development is unknown, in part due to the overlapping genesis and marker gene expression with other embryonic blood progenitors. Using single-cell transcriptomics, we define gene signatures that distinguish nascent HSCs from embryonic blood progenitors. Applying a lineage-tracing approach to selectively track HSC output *in situ*, we find

*Correspondence: teresa.bowman@einsteinmed.org.

AUTHOR CONTRIBUTIONS

Conceptualization, T.V.B., B.A.U., and S.S.H.; methodology, T.V.B., B.A.U., S.S.H., K.S.P., A.N., A.L., M.M., S.G.P., J.C.F., M.F.N., and C.M.; investigation, T.V.B., B.A.U., S.S.H., A.N., and J.C.F.; writing – original draft, T.V.B., B.A.U., and S.S.H.; writing – review & editing, T.V.B., B.A.U., K.S.P., and C.M.; funding acquisition, T.V.B. and B.A.U.; supervision, T.V.B.

DECLARATION OF INTERESTS

The authors declare no competing interests.

INCLUSION AND DIVERSITY

One or more of the authors of this paper self-identifies as an underrepresented ethnic minority in science. One or more of the authors of this paper received support from a program designed to increase minority representation in science.

SUPPLEMENTAL INFORMATION

Supplemental information can be found online at https://doi.org/10.1016/j.celrep.2021.109703.

significantly delayed lymphomyeloid contribution. An inducible HSC injury model demonstrates a negligible impact on larval lymphomyelopoiesis following HSC depletion. HSCs are not merely dormant at this developmental stage, as they showed robust regeneration after injury. Combined, our findings illuminate that nascent HSCs self-renew but display differentiation latency, while HSC-independent embryonic progenitors sustain developmental hematopoiesis. Understanding these differences could improve *de novo* generation and expansion of functional HSCs.

In brief

Ulloa et al. demonstrate that nascent HSCs robustly regenerate but display differentiation latency, while HSC-independent embryonic progenitors sustain developmental hematopoiesis. Their findings have implications for dissecting the programs underlying the genesis of bona fide HSCs.

Graphical Abstract

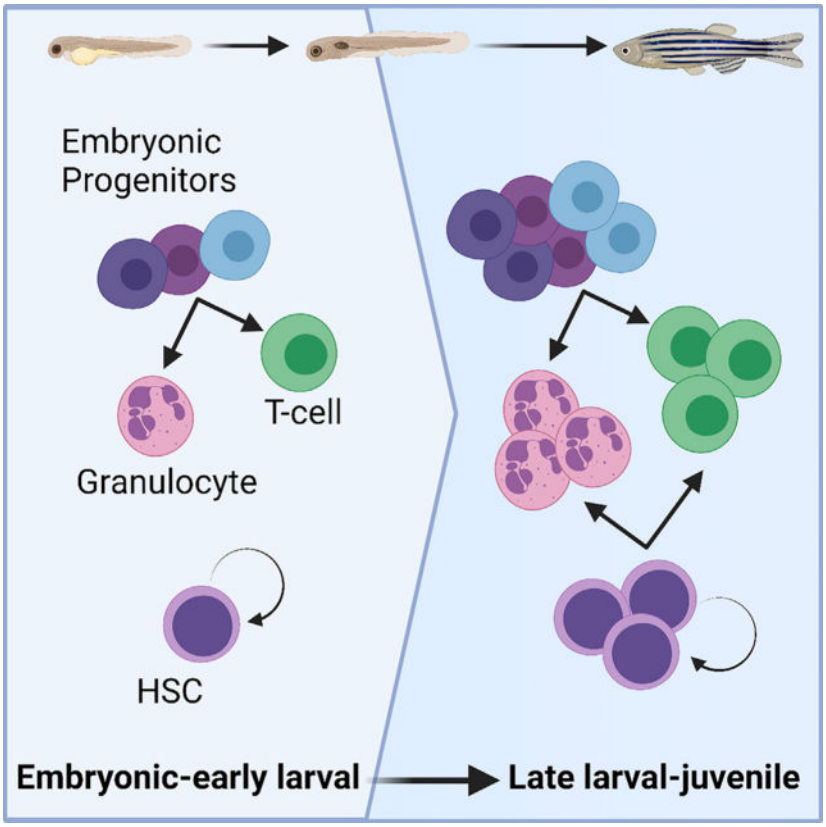

INTRODUCTION

Hematopoietic stem cells (HSCs) are defined by extensive self-renewal capacity and multilineage differentiation potential. They maintain lifelong hematopoiesis via the production of mature blood cells of the erythroid, myeloid, and lymphoid lineages (Chapple et al., 2018; Höfer et al., 2016). The regenerative ability of HSCs to replace a damaged hematopoietic system makes them clinically valuable for hematologic cell

replacement therapies (Baron and Storb, 2006). Although more than 50,000 hematopoietic cell transplantations occur worldwide each year (Aljurf et al., 2019), transplantation is not an option for all patients due to a paucity of appropriate donor cells (Fraint et al., 2021). Abilities to expand existing donor HSCs or to generate *de novo* cells from less limited stem cell sources such as pluripotent stem cells could conceivably increase transplantation opportunities. Understanding the earliest establishment of HSC self-renewal and multipotency properties could facilitate the development of methods to improve and maximize their therapeutic potential.

HSCs first emerge from the hemogenic endothelium of the newly formed dorsal aorta during embryogenesis (Boisset et al., 2010; Kissa and Herbomel, 2010). In addition to HSCs, other HSC-independent multi-lineage progenitors emerge in development, including erythroid-myeloid progenitors (EMPs) and lymphoid-myeloid progenitors (LMPs) (He et al., 2020b; Stachura and Traver, 2016; Chen et al., 2011). Limited in their self-renewal and differentiation output, these progenitors are mostly regarded as transient in nature (Waas and Maillard, 2017; Stachura and Traver, 2016; Chen et al., 2011). Seminal work revealed that HSC-independent embryonic progenitors were necessary and sufficient to sustain embryonic hematopoiesis (Chen et al., 2011). If transient embryonic progenitors can generate erythroid, myeloid, and lymphoid cells, what do HSCs contribute to embryonic/prenatal hematopoiesis? A difficulty in addressing this question is the spatially and temporally overlapping yet independent generation of HSCs and HSC-independent progenitors and their shared expression of several marker genes used for cell isolation (Zhan et al., 2018; Tian et al., 2017; Stachura and Traver, 2016; Chen et al., 2011; Davidson and Zon, 2004). Consequently, higher resolution data on the distinct transcriptional landscapes of hematopoietic stem and progenitor cell (HSPC) subsets are needed in combination with functional assays to examine their endogenous function in development.

Here, we conducted single-cell RNA sequencing (scRNA-seq) of newly emerged HSPCs isolated from developing zebrafish and identified seven distinct cell-type clusters corresponding to HSCs and three progenitor trajectories. From these studies, we identified temporally dynamic activity of transgenic reporters driven by the regulatory elements of the zebrafish *draculin* (*drl*) gene that distinguished HSCs from embryonic progenitors. Taking advantage of this difference, we applied a fluorescence-based lineage labeling method to selectively mark HSCs *in vivo* and found that lymphoid and myeloid differentiation from nascent HSCs is significantly delayed as compared to embryonic progenitors. Consistent with this result, we demonstrated a negligible impact on lymphoid and myeloid cell numbers in zebrafish larvae following *in situ* HSC depletion using an inducible larval HSC injury model. In contrast, HSCs robustly regenerated following depletion, suggesting they are not completely dormant at this developmental stage. Combined, our data demonstrate that while nascent HSCs possess self-renewal capacity, it is the HSC-independent embryonic progenitors that maintain early developmental hematopoiesis.

RESULTS

scRNA-seq revealed distinct embryonic progenitor and HSC clusters

To understand the complexity of HSPC heterogeneity, we used zebrafish as a representative vertebrate model to conduct 10X Genomics scRNA-seq analysis of enriched HSPC populations. We selected cells based on expression of known blood markers *drl* (Mosimann et al., 2015; Herbomel et al., 1999) and *runx1* (Tamplin et al., 2015). The *drl* gene acts as a pan-lateral plate mesoderm marker from gastrulation to early somitogenesis and is subsequently one of the earliest markers expressed in the developing hematopoietic system (Mosimann et al., 2015; Herbomel et al., 1999). Transgenic *drl* reporters, including *drl:mCherry* (driven by the 6.35-kb regulatory region of the *drl* gene) mark both long-lived HSCs and circulating erythrocytes in zebrafish (Prummel et al., 2019; Henninger et al., 2017; Robertson et al., 2016; Mosimann et al., 2015). To selectively analyze HSPCs, we isolated *drl:mCherry*$^{+}$ cells that were negative for the erythroid marker *gata1:GFP* (Traver et al., 2003; Long et al., 1997; Figures 1A and S1A; Table S1). We analyzed duplicate samples of *drl:mCherry*$^{+}$;*gata1:GFP*$^{-}$ cells (referred to hereafter as *drl*$^{+}$*gata1*$^{-}$) isolated from zebrafish embryos at 30 and 52 h post-fertilization (hpf) (referred to hereafter as 1 and 2 days post-fertilization [dpf], respectively) to span peak time points of HSC emergence and initial maturation (Henninger et al., 2017). We also performed scRNA-seq on *runx1+23:nls-mCherry*$^{+}$ (referred to hereafter as *runx1:mcherry* or *runx1*$^{+}$) cells isolated from 2 dpf embryos as a secondary marker for validation (Figure S1B; Table S1). We chose *runx1:mCherry* as a secondary marker to validate the *drl:mCherry* results, because this regulatory element (*runx1+23*) is documented to be most active in murine and zebrafish HSCs (Tamplin et al., 2015; Nottingham et al., 2007). Moreover, the zebrafish embryonic cells labeled by *runx1:mCherry* were shown to contain transplantable HSCs (Tamplin et al., 2015).

After batch correction (Haghverdi et al., 2018), we used uniform manifold approximation and projection (UMAP) to reduce the dimensionality of our data (Hao et al., 2020 Cao et al., 2019; McInnes et al., 2018). Focusing on 1 and 2 dpf *drl*$^{+}$*gata1*$^{-}$ cell populations, we conducted unsupervised clustering and identified 10 major clusters, in line with a heterogeneous HSPC pool at these developmental stages (Figure 1A). Comparison of the 2 dpf *drl*$^{+}$*gata1*$^{-}$ and *runx1*$^{+}$ scRNA-seq data revealed a significant overlap between the populations identified, confirming that our observed heterogeneity within the embryonic HSPC pool was not a consequence of the markers used but rather an indication of the complexity of developmental hematopoiesis (Figure S1C).

We designated the identities of the cell clusters (C) based on signature marker gene expression as defined in zebrafish and murine developmental hematopoiesis (Figures 1B and 1C). C5 was designated as pre-hemogenic endothelial cells (pre-HEs), as it featured strong expression of pan-endothelial genes (*kdrl, etv2*, and *cdh5*) (Bonkhofer et al., 2019; Oh et al., 2015; Sauteur et al., 2014), minimal expression of hemogenic endothelial cell (HE) marker genes (*lmo2, tal1*, and *meis1b*) (Wang et al., 2018; Patterson et al., 2007), and absent expression of HSC genes *gata2b* (Butko et al., 2015) and *myb* (Zhang et al., 2011). Thus, C5 represents a cell population initiating an endothelial-to-hematopoietic transition

(Zovein et al., 2008). In contrast, C6 cells had high expression of key hemogenic and HSC marker genes, including *gata2b*, *meis1b*, and *myb*, as well as expression of lineage-restricted genes indicative of multipotent priming, such as *gata1a* (erythroid) (Gutiérrez et al., 2020; Galloway et al., 2005), *ikzf1* (lymphoid) (Huang et al., 2019; Willett et al., 2001), and *coro1a* and *csf1rb* (myeloid) (Li et al., 2012; Carstanjen et al., 2005; Song et al., 2004); we consequently designated cluster C6 as hemogenic endothelial cells generating HSCs (HE/HSCs). The C4 cells expressed erythroid and lymphoid markers with low expression of myeloid markers, suggesting this population is analogous to the recently described lympho-erythroid-primed progenitor (LEP) in zebrafish (Kasper et al., 2020). Cells with LMP expression profile occurred in two clusters: (1) an LMP population with higher macrophage marker expression (*csf1ra, irf8, mfap4*, and *mpeg1.1*) (Rojo et al., 2019; Li et al., 2011; Zakrzewska et al., 2010) (LMP-M, C8) and (2) an LMP population with higher granulocyte marker expression (*mpx* and *lyz*) (Hall et al., 2007; Renshaw et al., 2006) (LMP-G; C9). The C7 and C10 clusters were highly similar and expressed progenitor-associated genes, including *meis1b* and *tcf12*, and mainly lymphoid-associated genes, including *tox* and *cd81a*, suggesting C7 and C10 represent more restricted lymphoid progenitors (LyPs). Most cells resided in clusters C1, C2, and C3 and predominantly expressed erythroid markers, which we broadly designated as erythroid progenitors (EryPs). Together, our identified clusters encompass the range of HSPC-associated progenitor traits (Hou et al., 2020; Kasper et al., 2020; Zhu et al., 2020; Xue et al., 2019; Zhou et al., 2016), here resolved into distinct progenitor clusters.

We inferred the developmental lineage trajectories of the different cell types from calculated RNA velocities using scVelo (Bergen et al., 2020; Figure 1D). We identified the same cell-type classifications using this analysis as we observed with the original Monocle3 clustering (Figure S1D). RNA velocity projections documented stochastic cell states between the LMP-M and LMP-G cells with a separation between LMPs and the other populations (Figure 1D). In this cluster projection, the pre-HE is a common precursor giving rise to three potential differentiation trajectories, HE/HSC, LyP, or LEP, suggesting a developmental connection among these cell states. The data also support a differentiation trajectory of a subset of LEPs to become more restricted EryPs. These progressions are further supported by pseudotime analysis using Monocle3 (Cao et al., 2019; Trapnell et al., 2014; Figure S1E). To give directionality to the pseudotime trajectory, we defined the pre-HE as the classical starting point of differentiation. Based on this analysis, the LEP and EryP represent more committed differentiated states.

To gain insights into functional features of the transcriptomes defining our 10 clusters, we took the most highly and selectively expressed marker genes (fraction of cells expressing the gene within the cell group >10% and marker test p value < 0.00005) for each cluster and conducted gene network enrichment analysis using Metascape (Figures 1E and 1F; Table S2; Zhou et al., 2019). The pre-HE cluster genes were enriched for terms related to vasculature development, cytoplasmic ribosomal proteins, cell migration, and hematopoiesis (Figure 1E). HE/HSC cluster genes showed enrichment in ribosomal biogenesis and tumor necrosis factor alpha signaling via nuclear factor κB signaling pathway, which has been associated with HSC development (Espín-Palazón et al., 2014; Figure 1F). The LyP cluster genes showed strong enrichment for dorsal aorta development, Notch signaling pathway, lymphoid

organ development, and regulation of cell differentiation (Table S2). As predicted, the LMP populations were enriched for both myeloid and lymphoid pathways, such as for myeloid leukocyte differentiation/activation, macrophage chemotaxis, and T cell receptor signaling pathway. Lastly, LEP and EryP populations were both enriched for erythrocyte signatures as well as cell cycle. Taken together, gene set enrichment network analysis supports our cell-type classifications and highlight important signatures for HSPC development and lineages as captured in our scRNA-seq dataset.

HSPC development is highly conserved between zebrafish and mammals (Avagyan and Zon, 2016; Robertson et al., 2016). To assess the similarity of the HE/HSC gene signatures in zebrafish and mammals, we compared our data to gene signatures defined in recently published HE and pre-HSC/HSC scRNA-seq experiments from the analogous developmental time points in mice (Hou et al., 2020; Vink et al., 2020; Zhu et al., 2020; Zhou et al., 2016; Table S3). We evaluated the relative aggregate gene expressions (gene-set score) of murine pre-HE (Zhu et al., 2020) and HE/pre-HSC/HSC signatures (Hou et al., 2020; Vink et al., 2020; Zhu et al., 2020 Zhou et al., 2016) across our zebrafish HSPC clustering (Figures S1F and S1G). The murine pre-HE gene-set score faithfully recapitulated our classification of the zebrafish pre-HE cluster (Figure S1F). Although the murine HE/HSC gene-set score had generalized coverage throughout the zebrafish cell types, the highest values were in the HE/HSC zebrafish cluster (Figure S1G). The HE/HSC gene-set score indicates that many of the genes expressed in this population are also expressed by other cell types and suggests our progenitor populations (LEPs, LMPs, EryPs, and LyPs) arose from HE. The LMP population (LMP-G and LMP-M) also had a relatively high gene-set score for both pre-HE and HE murine signatures, which could again suggest their pre-HE/HE origin. Overall, our results support that our zebrafish pre-HE and HE/HSC clusters are conserved with previous mammalian scRNA-seq signatures and illustrates the complexity of deciphering the heterogeneous pre-HSC/HSC compartment at this early developmental window.

Temporal regulation of the *drl:mCherry* reporter distinguishes HSPC subsets

We posited that the overlapping waves of HSPCs (Tian et al., 2017; Stachura and Traver, 2016; McGrath et al., 2015) may lead to differences in their prevalence over time. Therefore, we investigated the HSPC composition over the 1 and 2 dpf time frame (Figure 2A). We collected a greater number of EryP and HE/HSCs at 2 dpf as compared to 1 dpf (Figures 2A and 2B; Table S4). The EryP population also far outnumbered any of the other cell types at 2 dpf; in contrast, we observed a substantial decrease in the number of pre-HE cells, LyPs, LEPs, and LMPs at this later time point. In the *drl:mCherry* fish, expression of *mCherry* is a surrogate estimate for the *drl* regulatory element activity. Upon examination of the *drl:mCherry* transgene expression, we noticed high *mCherry* transcript levels in several HSPC subsets at 1 dpf, including pre-HE, HE/HSC, EryP, and LEP, but this became largely restricted to HE/HSCs and a portion of the EryP subset by 2 dpf. Based on these data, we posited that we could exploit the temporal differences in *drl*-driven transgene expression as a tool to distinguish HSCs from other non-EryPs.

The *drl* regulatory elements consist of an early pan-lateral plate mesodermal enhancer and two later-acting, cardiovascular-specific regulatory elements that confine *drl* reporter expression to the heart, endothelium, and blood lineages starting in late somitogenesis (Prummel et al., 2019). Previously, the *Tg(drl:creER^{T2})* transgenic zebrafish that permits 4-OH-tamoxifen (4-OHT)-inducible Cre activation was used to demonstrate that, in hematopoiesis, embryonic *drl*-expressing cells contribute to lifelong blood production (Henninger et al., 2017). Only adult hematopoiesis was examined in that study, leaving the differentiation dynamics and lineage contributions of *drl*-expressing hematopoietic lineages during development untested. Taking advantage of this system, we performed a fluorescence-based lineage-tracing method to distinctly label progenitors and HSCs at 1 and 2 dpf and track their lineage output. In double-transgenic *Tg*(*drl:creER^{T2};ubi:loxP-GFP-loxP-mCherry*) (referred to hereafter as *drl:creER^{T2};ubi:Switch*) zebrafish, 4-OHT-inducible Cre recombination removes the GFP cassette from *ubi:Switch* in *drl* reporter-expressing cells, leading to permanent mCherry expression in *drl*$^{+}$ labeled cells and their progeny (Mosimann et al., 2011, 2015; Figure 2C). We then monitored mCherry-fluorescent cells via flow cytometry and fluorescence imaging to determine the contributions of distinct *drl*$^{+}$ HSPCs to developmental and adult hematopoiesis.

To induce recombination, we exposed embryos to either 4-OHT or ethanol (EtOH) vehicle control starting at 30 hpf to label embryonic hematopoietic progenitors and HSCs (hereafter referred to as Prog+), and at 54 hpf to label HSCs as per our scRNA-seq analysis (Figures 2B and 2C). Consistent with previous findings (Henninger et al., 2017), we validated that our lineage-tracing system was labeling long-term multipotent HSCs in both Prog+ and HSC cohorts by confirming the presence of mCherry^{+} progeny in erythroid, lymphoid, and myeloid cells in 3- to 4-month-old adult kidney marrow cells via flow cytometry (Traver et al., 2003; Figures 2C and 2D). We compared the recombination efficiency 1 day post-4-OHT exposure and demonstrated a similar mCherry^{+} percentage of Prog+− and HSC-labeling, indicating similar Cre recombination efficiency at both switch time points (30 and 54 hpf) that allows direct comparison of the output of Prog+ and HSC lineage tracing in embryos (Figure 2E). By comparing Prog+ and HSC mCherry^{+} cell frequencies using flow cytometric and fluorescence imaging quantification, we discovered significant differences in the expansion of mCherry^{+} progeny from Prog+ versus HSCs over time, such as Prog+ progeny significantly outnumbering HSC progeny at 4 and 5 days post-labeling (Figures 2E and S2). This disparity suggests a potential difference in the contribution of HSC versus Prog+ progeny to developmental hematopoiesis that we more closely inspected in the next experiments.

Larval lymphoid and myeloid differentiation kinetics are distinct between HSCs and other embryonic progenitors

Based on the classical hematopoietic hierarchy (Stachura and Traver, 2016), we expected that mCherry^{+} progeny from HSC and Prog+ lineage tracing could either be replicative copies of the original labeled cell and/or differentiated mature lymphoid, myeloid, or erythroid cells. We focused on lymphoid and myeloid lineages and excluded analysis of erythroid cells because the *drl* promoter also directly labels EryP cells and mature erythrocytes, thus making it unclear if the lineage tracing in erythrocytes was HSC/Prog+

or erythrocyte derived (Henninger et al., 2017; Robertson et al., 2016; Mosimann et al., 2015). During vertebrate development, distinct hematopoietic cell types reside in particular anatomical locations at specific time points (Stachura and Traver, 2016). For example, erythrocytes and thrombocytes travel rapidly in circulation (Brönnimann et al., 2018 Khandekar et al., 2012); macrophages and dendritic cells can reside in the skin (Zhan et al., 2018); neutrophils ubiquitously spread throughout circulation, epidermis, or congregating in stressed tissue (Le Guyader et al., 2008); and T cells are abundant in the thymus (Tian et al., 2017). To measure Prog+ and HSC contribution to T lymphocytes, we imaged mCherry fluorescence in the thymus in 5–16 dpf larvae (Figure 3A). Prog+ cells contributed to thymic cells by 5 dpf (Figures 3B, 3D, and S3). In contrast, HSC contribution to the thymus was significantly delayed until after 7 dpf (Figures 3C, 3D, and S3). If the difference in lymphoid contribution was simply due to the 1-day delay in Cre activation, then we would expect a 1-day delay in contribution between Prog+ and HSCs. Instead, we observed more than a 2-day delay with thymus contribution not reaching a comparable level until 10 dpf, suggesting a functional difference in lymphoid differentiation between Prog+ and HSCs.

To examine HSC and Prog+ contribution to myeloid cells, we combined our lineage labeling system with a *Tg(mpx:GFP)* (Renshaw et al., 2006) line to mark granulocytes, generating triple-transgenic *drl:CreER^{T2};mpx:GFP;ubi:Switch)* zebrafish (Figure 4A). Fluorescence imaging of *Tg(mpx:GFP;ubi:Switch)* demonstrated that *mpx:GFP*$^{+}$ cells were brighter than the more diffuse *ubi:Switch* GFP signal (Figure 4B). Flow cytometry analysis confirmed that *drl:creER^{T2};mpx:GFP;ubi:Switch* larvae contain a unique GFP^{high} fraction that is absent in *drl:CreER^{T2};ubi:Switch* but with the same fluorescence intensity as *mpx:GFP*^{high} cells in *mpx:GFP* single transgenics (Figures 4C and S4). Thus, the mCherry^{+} cells within this *mpx:GFP*^{high} fraction represent myeloid progeny from *drl*+ cells (Figure 4C). Using this system, we found that HSC contribution to granulocytes was not appreciable until after 7 dpf, while Prog+ cells robustly generated myeloid progeny by 5 dpf (Figure 4D). As seen in our lymphoid results, myeloid contribution by Prog+ and HSCs reached comparable levels by 10 dpf. Consistent with a distinct function of Prog+ cells and HSCs, the lag in generating granulocytes was again greater than the expected 1-day difference if simply a consequence of delayed Cre activation. Together, these data demonstrate that embryonic and early larval hematopoiesis, including T cells and granulocytes, are sustained by an embryonic progenitor pool and not by HSCs.

HSCs regenerate following induced larval hematopoietic injury

Our lineage-tracing data suggest that HSCs do not significantly contribute to larval lymphomyelopoiesis (Figures 3 and 4). To assess if nascent HSCs are completely dormant at these early developmental stages, we developed an *in situ* larval hematopoietic regeneration assay. Adult HSC regenerative properties are routinely measured following myeloablative injuries such as chemotherapy or irradiation. Such approaches are not employable during development, as all tissues are highly proliferative and thus susceptible to cell death following these treatments. The nitroreductase/metronidazole (NTR/MTZ) system is commonly used in zebrafish to direct conditional and inducible cell ablation (Curado et al., 2008). NTR is a bacterial enzyme that metabolizes the pro-drug MTZ into a toxic DNA cross-linking intermediate leading to apoptotic cell death. We generated transgenic

zebrafish that express a cyan fluorescent protein (CFP)-NTR fusion under the control of the *drl* regulatory elements to drive observable NTR expression during early developmental hematopoiesis and to enable temporally controlled HSC depletion (Figure 5A). Harnessing the positional variability in Tol2-based transgene activity common to zebrafish transgenesis (Suster et al., 2009), we selected the resulting *Tg(drl:CFP-NTR)* (subsequently called *drl:CFP-NTR)* for high hematopoietic expression and comparatively low activity in other *drl*-expressing lineages such as the heart to minimize MTZ-induced cell ablation outside hematopoietic lineages. We confirmed the overlap between *drl:mCherry* and *drl:CFP-NTR*, demonstrating faithful expression of the *CFP-NTR* transgene (Figure S5A).

The caudal hematopoietic tissue (CHT) is a major site of larval hematopoiesis (equivalent to the mammalian fetal liver) (Murayama et al., 2006). We detected strong CFP-NTR fluorescent signal in the CHT region in both circulating and stationary cells from 1 to 8 dpf (Figure S5B). Exposure of *drl:CFP-NTR* embryos to MTZ at 1 dpf to target Prog+ cells resulted in significant mortality and severe cardiac edema from heart and vascular injury in larvae by 5 dpf (Figures S5C and S5D). This result is expected as *drl* is a pan-lateral plate mesoderm marker from gastrulation to early somitogenesis and subsequently refines to cardiovascular lineages, including cardiac progenitors and blood vessels in addition to blood (Mosimann et al., 2015). In generating the *drl:CFP-NTR* transgenic line to study hematopoietic regeneration, we selected for lines that reduced or turned off transgene expression in the heart and vessels by 2 dpf as judged by CFP fluorescence. Thus, treatment at 2 dpf, which would target HSCs, showed 100% larval survival and no edema. Control *drl:mCherry* embryos treated with MTZ showed similar mCherry^{+} fluorescence levels and survival as DMSO-treated controls, indicating that MTZ alone does not contribute to significant hematopoietic injury in our system. MTZ treatment of *drl:CFP-NTR* embryos at 2 dpf successfully depleted *drl:mCherry*$^{+}$ cells (Figures 5B and 5C). We observed significantly fewer circulating and stationary *drl:mCherry*$^{+}$ cells in the MTZ-treated experimental group compared to the DMSO- and MTZ-treated controls by 3–4 dpf (or 1–2 days post-MTZ treatment [dpM]).

Our *drl*-based NTR/MTZ system enables the study of HSC regeneration within the endogenous developmental environment. We confirmed that HSCs became depleted in the NTR/MTZ system at 2 dpf by using (1) *runx1:mCherry* zebrafish that express mCherry in HSCs (Tamplin et al., 2015) and (2) *cd41:eGFP* transgenics that express eGFP in HSCs as well as prothrombocytes and differentiated thrombocytes (Lin et al., 2005). Larval *runx1:mCherry*$^{+}$ HSCs express *drl:CFP-NTR*, as confirmed by confocal microscopy (Figure 5D). Using flow cytometry, we demonstrated a significant depletion of the *runx1:mCherry*$^{+}$ HSCs at 3 dpf (1 dpM) and a recovery of this population by 6 dpf (4 dpM) as compared to our control groups (Figures 5E and 5F). We confirmed the same ablation and regeneration dynamics in *drl:CFP-NTR;cd41:*eGFP double-transgenic embryos (Figures S5E and S5F). We observed that the nadir of depletion of *cd41:eGFP*$^{+}$ cells occurs at 3–4 dpf (1–2 dpM), with some recovery beginning at 5–6 dpf (3–4 dpM). Although significantly decreased at the nadir of depletion, the HSC population is not completely ablated using this NTR/MTZ system (Figures 5B, 5C, 5E, 5F, S5E, and S5F), allowing for their recovery. Altogether, these data indicate that embryonic HSCs can regenerate in response to hematopoietic injury.

HSC depletion minimally impacts myeloid and lymphoid maintenance after hematopoietic injury in early developmental stages

Based on our lineage labeling results, we found that HSCs are not actively contributing to early myeloid and lymphoid larval hematopoiesis (Figures 3 and 4). We therefore hypothesized that HSC depletion would not affect the maintenance of these lineages during early development as Prog+ predominantly or even exclusively form these lineages. To address this, we examined the levels of *rag2:mCherry*$^{+}$ lymphoid cells (Harrold et al., 2016) and *lysozyme:dsRed*$^{+}$ (*lyz*) myeloid cells (Hall et al., 2007) following HSC depletion. We predicted that if HSCs do play an essential role in early blood production, then their depletion following MTZ treatment would lead to fewer HSC-derived progenitors and ultimately fewer *rag2:mCherry*$^{+}$ and *lyz:dsRed*$^{+}$ mature cells in larvae.

In zebrafish, T lymphocyte progenitors colonize the embryonic thymus by 68 hpf and begin to express *rag2* at 72 hpf (Langenau et al., 2004; Trede and Zon, 1998). We found no overlap between the lymphocyte marker *rag2:mCherry* and *drl:CFP-NTR* expression in the thymus of 5 dpf zebrafish, confirming T cells would not be directly affected by MTZ treatment (Figure 6A). After HSC depletion with MTZ at 2 dpf, we monitored *rag2:mCherry* levels in double-transgenic *drl:CFP-NTR;rag2:mCherry* embryos from 3–6 dpf (1–4 dpM) using fluorescence imaging of the thymus and flow cytometry analysis (Figure 6B). By imaging-based analysis, we found MTZ-treated *drl:CFP-NTR*$^{+}$*;rag2:mCherry*$^{+}$ embryos had slightly diminished seeding of the thymus at 3–4 dpf (1–2 dpM) with recovery by 5–6 dpf (3–4 dpM) (Figures 6C and 6D). However, quantification of T cell frequency by flow cytometry revealed minimal to no decrease of the *rag2:mCherry*$^{+}$ cells after HSC depletion (Figures 6E and 6F). Consistent with our lineage-tracing data, this comparably subtle effect suggests that HSCs have little contribution to larval T lymphocyte production by 6 dpf.

The *Tg(lyz:dsRed)* reporter labels lysozyme-C-producing cells, mainly granulocytes and some macrophages (Hall et al., 2007). Similar to lymphoid cells, we found little to no apparent overlap in fluorescence between *drl:CFP-NTR*$^{+}$ cells and *lyz:dsRed*$^{+}$ granulocytes (Figure 7A). To measure the effect of HSC depletion on granulocyte levels, we treated double-positive *drl:CFP-NTR;lyz:dsRed* embryos with MTZ at 2 dpf and monitored the lyz-expressing cells using fluorescence imaging and flow cytometry (Figure 7B). When imaging the CHT region, we observed a minor decrease of granulocytes with a nadir at 4 dpf (2 dpM) and a full recovery by 6 dpf (4 dpM) as compared to controls (Figures 7C and 7D). When monitoring the total *lyz:dsRed*$^{+}$ cell population using flow cytometry, we found no significant differences between controls and the experimental group (Figures 7E and 7F). Again, this comparably mild effect of *drl:CFP-NTR*$^{+}$ cell depletion on *lyz:dsRed*$^{+}$ cells suggests that HSCs do not significantly contribute to larval myelopoiesis up to 7 dpf, consistent with our lineage-labeling data.

These data further confirm that HSCs can regenerate after depletion during embryonic stages and that their depletion has a minor to no impact on larval lymphomyelopoiesis that is driven by Prog+ cells. Combined, our findings document that HSC-independent progenitors, and not HSCs, sustain embryonic hematopoiesis.

DISCUSSION

A main challenge of studying developmental HSC contribution originates from the difficulty of specifically distinguishing HSCs from embryonic hematopoietic progenitors, as their emergence is spatiotemporally overlapping and commonly used markers are expressed in both developing progenitor and HSC populations (Kasper et al., 2020; Hadland and Yoshimoto, 2018; McGrath et al., 2015; Chen et al., 2011; Godin and Cumano, 2002). Through our scRNA-seq exploration of newly formed HSPCs, we document transcriptional heterogeneity that defines seven distinct HSPC populations, including well-documented subsets, such as pre-HE, HE/HSC, and EryP, and new populations, such as LMP (He et al., 2020a) and LEP (Kasper et al., 2020; Figure 1). This high-resolution transcriptional landscape of developmental HSPCs allowed us to infer differentiation trajectories and cell-type-specific gene enrichment networks relevant to early hematopoiesis.

Akin to recent murine scRNA-seq analyses, we have captured pre-HE and HE cells (Zhu et al., 2020; Zhou et al., 2016). This pre-HE transition state shows upregulation of vasculature gene expression while also showing stronger enrichment for hematopoietic development markers. Moreover, we have shown that pre-HEs can give rise to cells with distinct development trajectories. However, unlike Zhu et al. (2020) who found two different murine hematopoietic waves (an initial lymphomyeloid-biased progenitor followed by pre-HSC precursors; Zhu et al., 2020), we discovered at least three distinct trajectories arising from pre-HE cells in zebrafish: HSCs, LyPs, and LEPs (Figure 1D). Similar to our HE/HSC enrichment analysis, recent murine scRNA-seq analysis also revealed that ribosome pathway terms are upregulated upon hemogenic specification (Hou et al., 2020). Proteostasis is now emerging as a major player in the life and health of HSCs, and together, these findings suggest this could be an HSC-defining property. The granularity with which HSCs and embryonic progenitors are distinguished from each other in our scRNA-seq analysis offers the first comprehensive transcriptomic look into what drives their separation in zebrafish.

Our data support that *drl*-driven transgenes are expressed in HSCs, which is consistent with previous findings of transplantable long-term *drl*+ HSCs (Henninger et al., 2017). In addition, our data show that *drl*-driven expression in HSC-independent progenitors fades beyond 1 dpf (Figure 2B). This conclusion is supported not only by the scRNA-seq data but also by the functional experiments of lineage tracing and the larval hematopoietic regeneration assay. The functional differences revealed by the temporal lineage-tracing experiments (Prog+ and HSC) demonstrated that the cells labeled at 1 and 2 dpf had distinct lymphomyeloid differentiation capacities and kinetics (Figures 3 and 4). We leveraged our combined data using multiple approaches as well as published data to draw the conclusions regarding the cell types marked by *drl*-driven transgene expression. The ability to isolate HSCs from other HSC-independent progenitors allowed for the extensive analysis into their self-renewal and differentiation potential in development.

That HSCs have a delayed hematopoietic contribution during development indicates a disconnect between the timing of HSC emergence and their demonstrable long-term function. Additionally, our data contrast the classically held interpretation that HSCs reside at the top of the hematopoietic hierarchy, maintaining lifelong erythroid, myeloid, and

lymphoid hematopoiesis (Kobayashi et al., 2019). Since nascent HSCs can engraft and reconstitute the blood system of a transplanted host, it was posited that they were the source of all blood cells from shortly after their emergence onward (Medvinsky and Dzierzak, 1996). Nonetheless, seminal work in mice and zebrafish has indicated that embryonic hematopoietic progenitors, in the absence of HSCs, were necessary and sufficient for sustaining hematopoiesis in early life (Chen et al., 2011; Soza-Ried et al., 2010). These data suggested that HSCs did not significantly contribute to developmental hematopoiesis, but HSC contribution to differentiated blood lineages was not directly assessed. Although not fully explored in mammals, clonal tracing performed during fetal stages in the mouse has suggested that HSC clones do not robustly contribute to mature lineages until postnatal stages (Busch et al., 2015). Recent studies illustrated that yolk-sac-derived progenitors, and not HSCs, sustain erythropoiesis and create megakaryocyte progenitors throughout murine embryonic life (Iturri et al., 2021; Soares-da-Silva et al., 2021). In developing zebrafish, T cell-producing LyP (Tian et al., 2017) and LMP populations (He et al., 2020a) were also recently identified to arise in development and represent distinct HSC-independent progenitors. These HSC-independent T cells were found to contribute to early thymic seeding by 5 dpf, while the presumed HSC-dependent wave contributed from 8 dpf and beyond (Tian et al., 2017). Consistent with these studies, we demonstrate that embryonic hematopoietic progenitors in zebrafish sustain early developmental hematopoiesis while HSCs do not detectably contribute until late larval lymphomyelopoiesis (Figures 3 and 4). Combined, these findings in zebrafish and murine models indicate a strong conserved differentiation latency of nascent HSCs spanning all hematopoietic lineages.

The observed differentiation latency itself could also denote the nascency or immaturity of HSCs. In adult organisms, injury-induced regeneration assays are often used to challenge HSCs to illuminate function. These approaches are mainly based on myeloablative injuries, such as chemotherapy or irradiation that target proliferating cells. Developing embryos are highly proliferative; thus, use of such treatments impairs overall development and organ formation. To investigate the potential for HSC regeneration and their temporal lineage contribution during development *in situ*, we here established an HSC-selective injury model based on transgenic *NTR* driven by the *drl* regulatory elements that permitted an assessment of HSC stress response during zebrafish ontogeny without transplantation. We delineated that HSCs regenerate following their depletion but that this hematopoietic injury had a negligible impact on developmental lymphomyelopoiesis, which is instead dependent on earlier hematopoietic progenitor cells (Figures 5, 6, and 7). The demonstration of HSC regeneration during development is consistent with studies in zebrafish and mice that show self-renewal capacity of embryonic HSCs upon transplantation (Tamplin et al., 2015; Ema and Nakauchi, 2000; Müller et al., 1994). Future studies using our developmental regeneration assay have the potential to provide insights into the spatiotemporal dynamics of HSC self-renewal and differentiation properties.

Together, our findings demonstrate that after their emergence, HSCs display differentiation latency but active self-renewal. Our data illustrate that the embryonic progenitors, not HSCs, sustain early developmental hematopoiesis. Understanding how and where HSCs might acquire the ability to sense and regenerate a challenged or damaged blood system during development will help guide improvements to generate functional HSCs from renewable

pluripotent stem cells. Additionally, studying HSC self-renewal and differentiation during ontogeny may help us delineate the factors that promote HSC expansion without loss of other functions.

STAR★METHODS

RESOURCE AVAILABILITY

Lead contact—Further information and requests for scripts, resources, and reagents should be directed to and will be fulfilled by lead contact, Teresa V. Bowman (teresa.bowman@einsteinmed.org).

Materials availability—Plasmids and animal models generated in this paper will be shared freely upon request to the lead contact.

Data availability

- The scRNA-seq data generated in this manuscript have been deposited at GEO: GSE182213 and are publicly available. Microscopy data reported in this paper will be shared by the lead contact upon request.
- This paper does not report original code.
- Any additional information required to reanalyze the data reported in this work is available from the lead contact upon request.

EXPERIMENTAL MODEL AND SUBJECT DETAILS

Zebrafish husbandry—Zebrafish were bred and maintained as described previously (Lawrence, 2011). All fish were maintained according to Institutional Animal Care and Use Committee (IACUC)-approved protocols in accordance with the Albert Einstein College of Medicine research guidelines.

Transgenic lines—Transgenic lines used in this study included *Tg(drl:mCherry)* (Sánchez-Iranzo et al., 2018), *Tg(gata1:eGFP)* (Shafizadeh et al., 2004), *Tg(runx1+23:nls-mCherry)* [shortened to *Tg(runx1:mCherry)*] (Tamplin et al., 2015), *Tg(mpx:GFP)* (Renshaw et al., 2006), *Tg(cd41:eGFP)* (Lin et al., 2005), *Tg(rag2:mCherry)* (Harrold et al., 2016), and *Tg(lyz:dsRed)* (Hall et al., 2007). For the lineage tracing experiments, we used *Tg(drl:creER^{T2})* (Mosimann et al., 2015), *Tg(ubi:loxP-GFP-loxP-stop-mCherry)* [also known as *Tg(ubi:Switch)*] (Mosimann et al., 2011), and *Tg(mpx:GFP;ubi:Switch)*, which are the progeny of *Tg(mpx:GFP)* (Renshaw et al., 2006) crossed to *Tg(ubi:Switch)*.

The *drl:CFP-Nitroreductase* (*NTR*) construct was generated using multisite gateway cloning. The *drl* regulatory elements in pCM296 as pENTR5′ vector (Mosimann et al., 2015), *CFP-NTR* construct (Curado et al., 2007), α-*crystallin:YFP*-carrying *pDestCY* backbone *pCM326* (Mosimann et al., 2015) have been previously described. The construct and *Tol2* RNA (Kwan et al., 2007) were injected into one-cell stage embryos, which were then screened for correct CFP expression. Positive embryos were reared to adulthood and screened for positive *F0* founders. Single-insertion transgenic strains with persistent

expression of *drl:CFP-NTR* in only blood (and not dominantly expressed in the heart or endothelium) were specifically selected to prevent toxicity from injuring these essential tissues where *drl*-based transgenics can also be actively expressed (Prummel et al., 2019; Mosimann et al., 2015). Preferential hematopoietic expression (non-cardiac and non-vascular) was only found by 2 dpf in some transgenic lines; no restricted expression was found any earlier. All experiments were confirmed with at least two independent transgenic lines.

METHOD DETAILS

Embryo/larval fluorescence-activated cell sorting—Flow cytometry protocol was used to prepare *Tg(drl:mCherry;gata1:GFP)* (30 and 52 hpf) and *runx1:mCherry* (52 hpf) in replicate for fluorescent cell sorting prior to 10X Genomics scRNA-seq. For each group, 200–300 embryos were manually dissociated using a sterile razor blade. The material was then resuspended in 1 mL of 1x Dulbeccos-PBS (D-PBS) (Life Technologies) and digested with a 1:65 dilution of 5 mg/mL Liberase (Roche) for 6 minutes in a 37°C water bath. The reaction was stopped with the addition of 5% fetal bovine serum (FBS) (Life Technologies). The triturated suspension was then filtered twice through a 40 μm cell strainer (Falcon), pelleted by centrifugation, and resuspended in 2 mL of FACS buffer (0.9x D-PBS, 5% FBS, 1% Pen/Strep (Life Technologies)). DAPI (4’,6-diamidino-2-phenylindole, Sigma) was added to a final concentration of 1 μg/mL to exclude dead cells from the analysis. Gates for background signal were drawn using cells from non-fluorescent embryos (Figures S1A–B). For *Tg(drl:mCherry;gata1:GFP)*, we sorted mCherry-positive and GFP-negative cells at 1 and 2 dpf (28–30 and 50–52 hpf, respectively) in replicate to enrich for HSPCs and decrease the erythroid *gata1* signal. For *Tg(runx1:mCherry)*, we sorted for mCherry-positive cells at 2 dpf (50–52 hpf). Sorting was performed on a Becton Dickinson FACSAria which was equipped with a 100-micron nozzle, run at pressure 20 psi with flow rates less than 3,000 events/second. Sorted cells were collected into microcentrifuge tubes containing 500 μL IMDM + 10% FBS + 1% Pen/Strep at 4°C.

scRNA-Seq—Sorted cells were processed for library preparation using the 10X Genomics Chromium Single Cell 3′ Reagent Kit v3.1.0, performed by the Einstein Genetics Genomics Core. Libraries were then sent to Genewiz for sequencing. Initial sample quality control (QC) involved assessing library size on the Agilent TapeStation Analysis Software 3.2 (Agilent Technologies, Inc 2019), concentration measurement on Qubit dsRNA Assay, and final quantitation by qPCR. Indexed libraries were pooled and sequenced on an Illumina HiSeq paired-end 2 × 150 bp read length, single index with 5% PhiX spike-ins.

scRNA-seq data analysis

Preprocessing of scRNA-seq data: Sample alignment, filtering, barcode counting, and unique molecular identifier counting (UMI) were performed with 10x Genomics Cell Ranger 4.0.0 pipeline. Samples were aligned to a custom zebrafish reference genome (*Danio rerio* GRCz11/danRer11) that included *mCherry* and *GFP* sequences, built using the Cell Ranger cellranger *mkref* pipeline. We sequenced 25,574 cells of which 25,248 cells passed quality control using Cell Ranger, including 4,469 cells at 1 dpf (30 hpf) and 20,779 cells at 2 dpf (52 hpf). On average, 1804 and 676 genes were detected per cell at 1 and 2

dpf embryos, respectively. Cells that passed quality control metrics as defined by the Cell Ranger pipeline were passed into downstream clustering analysis. Summary statistics of quality control for analyzed cell populations can be found in Table S1.

Dimension reduction, unsupervised clustering, and cell type identification— Seurat (version 4.0) (Hao et al., 2020) and Monocle3 (Cao et al., 2019) were used to analyze merged *drl:mCherry*$^{+}$*;gata1:GFP*$^{-}$ samples (replicates for 1 dpf and replicates for 2 dpf). For Seurat, we preprocessed (nFeature_RNA 200–4500 and mitochondrial percentage < 5%), normalized, and selected 5,000 most variable genes to feed into dimension reduction by principal component analysis PCA. Then, the top 50 principal components were selected for uniform manifold approximation and projection (UMAP) reduction and clustering. The number of clusters is dependent on parameter resolution (0.5), from which we resolved 12 cluster groups. SeuratWrappers were used to convert into a Monocle3 cell dataset object, which we used for trajectory and top marker analysis. For Monocle3, we selected the top 50 dimensions for preprocessing using PCA method, and for dimensional reduction using UMAP with a resolution of 7e-5, by which the number of cluster groups were 10. Batch-correction (Haghverdi et al., 2018) was conducted prior to UMAP dimensional reduction by matching mutual nearest neighbors. For the overlap of *drl:mCherry*$^{+}$*;gata1:GFP*$^{-}$ and *runx1:mCherry*$^{+}$ samples at 2 dpf, the above protocol was also followed.

Cell types were assigned by key marker gene expression, as defined by literature search. Top marker analysis was conducted based on cell type assignments, up to 200 genes were chosen per group (criteria: fraction expressed in > 10% of cells and a test p value < 0.00005). Top markers derived for each cell type using Monocle3, as described above, were then used for pathway enrichment analysis with Metascape (Zhou et al., 2019).

HE/HSC zebrafish and murine comparison—In Seurat v4.0, we conducted differential expression (DE) analysis for upregulated genes (p > 3.89E-6, average log2FC > 0.693) in the HE/HSC cluster (c6) using non-parametric Wilcoxon rank sum test. This HE/HSC list of DE genes was compared to publicly available murine HE (Hou et al., 2020; Zhu et al., 2020) and pre-HSC/HSC (Vink et al., 2020; Zhu et al., 2020; Zhou et al., 2016) datasets. We converted the gene lists from these studies into their zebrafish homolog counterparts with online tool Ensembl BioMart. Code to derive gene set scores were provided by the Hadland lab. Single cell gene set scores were calculated as the log-transformed sum of the size factor-normalized expression for each gene in publicly available murine datasets: pre-HE (Zhu et al., 2020) and HE/HSC (Hou et al., 2020; Vink et al., 2020; Zhu et al., 2020; Zhou et al., 2016).

Differential trajectories—Cell Ranger output files for *drl:mCherry*$^{+}$*;gata1:GFP*$^{-}$ samples (replicates for 1 dpf and replicates for 2 dpf) were read into velocyto (La Manno et al., 2018) for the creation of .loom formatted files containing spliced, unspliced, and ambiguous counts. These reformatted data were merged and reprocessed in Seurat. Preprocessing, dimensional reduction with UMAP, and cell type identification were conducted as described above for the Seurat pipeline. Using this new cluster projection, we were able to identify the same cell types as before. SeuratWrappers and publicly available tutorials on Github

helped to create inferred lineage differentiation trajectories using RNA velocity (scVelo) and pseudotime analysis (Monocle3).

Lineage Tracing with Tg(ubi:Switch)—For lineage tracing experiments using *Tg(drl:creER^{T2};ubi:Switch)* or *Tg(drl:creER^{T2};mpx:GFP;ubi:Switch)*, embryos at 30 or 54 hpf were transferred to a Petri dish (150 mm x 15 mm) at a density of 40–50 embryos per plate. Embryo buffer was replaced with E3 embryo buffer (5 mM NaCl, 0.17 mM KCl, 0.25 mM $CaCl_2$, and 0.15 mM $MgSO_4$) containing 12 μM (Z)-4-Hydroxytamoxifen (4-OHT) (Sigma, H7904) or 0.05% (v/v) ethanol (EtOH) as a vehicle control (Henninger et al., 2017). Zebrafish were treated with 4-OHT or EtOH for 20 hours (30–50 hpf or 54–74 hpf) in a 28°C incubator. After treatment, embryos were washed three times with fresh embryo buffer and placed back in a 28°C incubator. From 5–16 dpf, larvae were transferred to the fish facility nursery where they were kept in fish water supplemented with methylene blue with E3 embryo medium at room temperature and fed paramecia twice daily.

Nitroreductase (NTR)/Metronidazole (MTZ) Assay—For assessing the impact of *drl*-cell depletion on the blood system and to determine co-expression of *drl:CFP-NTR* will specific cell types, *Tg(drl:CFP-NTR)* adult zebrafish were crossed to cell type-specific mCherry fluorescent transgenic lines or AB WT fish. At 24 hpf, the embryos were scored for both CFP and mCherry fluorescence. As the mCherry fluorescence is brighter than CFP, mCherry fluorescence was used to monitor the impact of *drl* cell depletion on each lineage. Cell type specific transgenic lines used were *drl-Tg(drl:mCherry)* (Sánchez-Iranzo et al., 2018), HSPC/thrombocytes-*Tg(cd41:eGFP)* (Lin et al., 2005), *HSPC-Tg(runx1:mCherry)* (Tamplin et al., 2015), granulocytes-*Tg(lyz:dsRed)* (Hall et al., 2007), and T cells-*Tg(rag2:mCherry)* (Harrold et al., 2016).

At 54 hpf (0 dpM), embryos were treated as such: *Tg(drl:CFP-NTR)*-positive embryos were treated with either 1% (v/v) DMSO or 10 mM MTZ (Sigma, M3761), and *Tg(drl:CFP-NTR)*$^{-}$ embryos were treated with 10 mM MTZ. Dilutions of DMSO or 1 M MTZ stock were made with E3 embryo medium. Embryos were then placed into 24-well plates (n = 15/well) with 2 mL of solution per well or in Petri dishes (150 mm x 15 mm, n = 40–50) with 25 mL of solution per plate and treated for 20 hours overnight in a 28°C incubator. Light exposure was avoided by wrapping the plates in foil as MTZ is light sensitive. Embryos were then washed twice with E3 water. Zebrafish were analyzed via fluorescence imaging and flow cytometry methods.

Fluorescent imaging—Live zebrafish embryos (54 hpf – 8 dpf) were anesthetized with 0.01% tricaine (Fisher), then mounted in 4%–6% (wt/vol) methylcellulose in 35-mm imaging dishes (MatTek) as described previously (Renaud et al., 2011). Fluorescent imaging of *Tg(drl:creER^{T2};ubi:Switch)*, *Tg(drl:CFP-NTR;drl:mCherry)*, *Tg(drl:CFP-NTR;cd41:GFP)*, *Tg(drl:CFP-NTR;lyz:dsRed)*, and *Tg(drl:CFP-NTR;rag2:mCherry)* were performed with Zeiss Discovery.V8 and Zeiss Axio Observer A1 Inverted microscope with an AxioCam HRc Zeiss camera and Zeiss Zen 2 or 2.5 software. Fluorescence was detected with cyan fluorescent protein (CFP), mCherry, Texas Red (for dsRed lines), and green fluorescent protein (GFP) filters.

A Zeiss Live DuoScan confocal microscope with AIM 4.2 Software was used to visualize co-expression in *Tg(drl:CFP-NTR^{+};runx1:mCherry^{+})* embryos using 405nm and 561nm excitation wavelength. Embryos (6 dpf) were anesthetized with 0.01% tricaine (Fisher), oriented in a drop of 3% wt/vol methylcellulose, then mounted in 1% agarose in 35-mm imaging dishes (MatTek) as described previously (Renaud et al., 2011).

Fluorescence Microscopy Image Analysis—Fluorescence microscopy images of the raw data were analyzed using FIJI (Schindelin et al., 2012). On each image, a region of interest (the fluorescent tissue within the CHT or thymus) was selected. Corrected Total Cell Fluorescence (CTCF) was calculated as Integrated density of region of interest - (Area of region of interest X Mean fluorescence of 3 to 6 different background regions). CTCF values of experimental embryos were normalized to that of the controls by dividing the CTCF value of an individual embryo's image by the average CTCF value of all the images from the control group. All data were then statistically analyzed (see below). Edematous embryos were not included in the analysis.

To determine the threshold for mCherry^{+} thymi in the lineage tracing analysis, 7 scientists blindly scored for mCherry^{+} thymi in 34 images of 5 and 10 dpf *Tg(drl:creER^{T2};ubi:Switch)* zebrafish previously treated with 4-OHT from 30–50 hpf or 54–74 hpf. The frequency at which each image was scored positive and negative among the scientists was calculated. Images that were scored positive more than 50% of the time were deemed to have a detectable mCherry^{+} thymus. We calculated the sensitivity and specificity of using CTCF cut-offs by this visual detection standard. A true positive (TP) was an image positively scored and having a CTCF above the cut-off; a false negative (FN) was an image positively scored but having a CTCF below the cut-off; a true negative (TN) was an image negatively scored and having a CTCF below the cut-off, and a false positive (FP) is an image negatively scored and having a CTCF above the cut-off. By plotting a receiving operative characteristics (ROC) curve, we determined a CTCF threshold (7.5) that would give us both an optimal sensitivity (TP/[TP+FN]) and specificity (TN/[TN+FP]) (Figure S6B).

The SparQ (Streamlined Particle Quantification) (Mesquita et al., 2020) software was used to automate the quantification of the fluorescence particles in the CHT region of *Tg(drl:CFP-NTR; cd41:GFP)* zebrafish.

Flow cytometry protocol and analysis—Flow cytometry analysis was conducted for *Tg(drl:creER^{T2};mpx:GFP;ubi:Switch)* as part of the lineage tracing assay from 2–16 dpf and for *runx1:mCherry*, *lyz:dsRed*, and *rag2:mCherry* as part of the NTR/MTZ regeneration assay from 2–9 dpf. For each group, 7–10 embryos were anesthetized with 0.01% tricaine (Fisher) and then dissociated using a sterile razor blade. The material was then resuspended in 600 μL of 1x Dulbeccos-PBS (D-PBS) (Life Technologies) and digested with a 1:65 dilution of 5 mg/mL Liberase (Roche) for 10–15 minutes in 37°C water bath. The reaction was stopped with the addition of 5% fetal bovine serum (FBS) (Life Technologies). The triturated suspension was then filtered through a 40 μm cell strainer (Falcon), pelleted by centrifugation, and resuspended in 300 μL of FACs buffer (0.9x D-PBS, 5% FBS, 1% Penn/Strep (Life Technologies)). DAPI was added to a final concentration of 1 μg/mL to

exclude dead cells from the analysis. Gates for background signal were drawn using cells from non-fluorescent embryos.

For adult kidney marrow analysis, kidneys from 3–4 months post fertilization zebrafish were dissected, resuspended in 500 μL of FACS buffer supplemented with 1 μg/mL DAPI, and filtered through a 40-μm cell strainer (Falcon). Forward and side scatter parameters were used to resolve the major blood cell lineages of erythroid, myeloid, lymphoid, and precursor, as previously described (Traver et al., 2003).

All samples were analyzed at the Flow Cytometry Core Facility at the Albert Einstein College of Medicine using an LSR II flow cytometer (BD Biosciences) and data was processed using FlowJo Software (versions 10.6 – 10.7.1).

QUANTIFICATION AND STATISTICAL ANALYSIS

Kaplan-Meier curve analysis and two-way ANOVA with Sidak's and Tukey's multiple comparisons tests were performed using GraphPad Prism (version 8). Experiments were performed with a minimum of three independent replicates. Error bars indicate standard deviation from mean, or as specified. ns, not significant; * $p < 0.05$; ** $p < 0.01$; *** $p < 0.001$; **** $p < 0.0001$.

Supplementary Material

Refer to Web version on PubMed Central for supplementary material.

ACKNOWLEDGMENTS

This work was funded by the American Cancer Society (grant RSG-129527-DDC), the DOD (grant BM180109), the NIH (grant 1R01DK121738), and the Edward P. Evans Foundation (T.V.B.); the NIH (grants T32GM007288 and F31HL152562) (B.A.U.); the Einstein SOARS program (S.S.H.); the American Australian Association Sir Rupert Murdoch Postdoctoral Fellowship (K.S.P.); The Einstein Training Program in Stem Cell Research funded by the Empire State Stem Cell Fund through New York State Department of Health contract C30292GG (K.S.P. and A.N.); NIH F31HD097901 (S.G.P.); NIH T32 GM007491 (M.F.-N.); and funds from the University of Colorado School of Medicine and the Children's Hospital Colorado Foundation (C.M.). Instrumental feedback to the growth of this project was provided by Britta Will, Kira Gritsman, Ulrich Steidl, and Sofia De Oliveira. We would like to thank several Einstein Core Facilities supported by NIH grant P30CA013330, including Flow Cytometry, Genomics, and Computational Genomics Facilities. For their assistance with cell sorting and flow cytometry analysis, we thank the Flow Cytometry core members Jinghang Zhang, Yu (Joey) Zhang, Fnu (Aodeng) Aodengtuya, and Ming Liu. Additionally, we would like to thank the Einstein Genomics Core and David Reynolds for their assistance with 10X Genomics scRNA pre-processing and library preparation. For their computational support, thank you to Tobias Schraink, the Einstein Computational Genomics Core, and Dr. Robert Dubin. For their animal support, we thank the Einstein Zebrafish core members Clinton de Paolo and Spartak Kalinin. Lastly, we greatly thank the Hadland lab and its members, especially Dr. Brandon Hadland and Tessa Dignum, for their guidance with scRNA-seq analysis and providing code.

REFERENCES

Aljurf M, Weisdorf D, Hashmi S, Nassar A, Gluckman E, Mohty M, Rizzo D, Pasquini M, Hamadani M, Saber W, et al. (2019). Worldwide Network for Blood and Marrow Transplantation Recommendations for Establishing a Hematopoietic Stem Cell Transplantation Program in Countries with Limited Resources, Part II: Clinical, Technical, and Socioeconomic Considerations. Biol. Blood Marrow Transplant. 25, 2330–2337. [PubMed: 31002990]

Avagyan S, and Zon LI (2016). Fish to Learn: Insights into Blood Development and Blood Disorders from Zebrafish Hematopoiesis. Hum. Gene Ther. 27, 287–294. [PubMed: 27018965]

Baron F, and Storb R (2006). Allogeneic hematopoietic cell transplantation following nonmyeloablative conditioning as treatment for hematologic malignancies and inherited blood disorders. Mol. Ther. 13, 26–41. [PubMed: 16280257]

Bergen V, Lange M, Peidli S, Wolf FA, and Theis FJ (2020). Generalizing RNA velocity to transient cell states through dynamical modeling. Nat. Biotechnol. 38, 1408–1414. [PubMed: 32747759]

Boisset J-C, van Cappellen W, Andrieu-Soler C, Galjart N, Dzierzak E, and Robin C (2010). In vivo imaging of haematopoietic cells emerging from the mouse aortic endothelium. Nature 464, 116–120. [PubMed: 20154729]

Bonkhofer F, Rispoli R, Pinheiro P, Krecsmarik M, Schneider-Swales J, Tsang IHC, de Bruijn M, Monteiro R, Peterkin T, and Patient R (2019). Blood stem cell-forming haemogenic endothelium in zebrafish derives from arterial endothelium. Nat. Commun. 10, 3577. [PubMed: 31395869]

Brönnimann D, Annese T, Gorr TA, and Djonov V (2018). Splitting of circulating red blood cells as an in vivo mechanism of erythrocyte maturation in developing zebrafish, chick and mouse embryos. J. Exp. Biol. 221, jeb184564. [PubMed: 29903841]

Busch K, Klapproth K, Barile M, Flossdorf M, Holland-Letz T, Schlenner SM, Reth M, Höfer T, and Rodewald HR (2015). Fundamental properties of unperturbed haematopoiesis from stem cells *in vivo*. Nature 518, 542–546. [PubMed: 25686605]

Butko E, Distel M, Pouget C, Weijts B, Kobayashi I, Ng K, Mosimann C, Poulain FE, McPherson A, Ni CW, et al. (2015). Gata2b is a restricted early regulator of hemogenic endothelium in the zebrafish embryo. Development 142, 1050–1061. [PubMed: 25758220]

Cao J, Spielmann M, Qiu X, Huang X, Ibrahim DM, Hill AJ, Zhang F, Mundlos S, Christiansen L, Steemers FJ, et al. (2019). The single-cell transcriptional landscape of mammalian organogenesis. Nature 566, 496–502. [PubMed: 30787437]

Carstanjen D, Yamauchi A, Koornneef A, Zang H, Filippi M-D, Harris C, Towe J, Atkinson S, Zheng Y, Dinauer MC, and Williams DA (2005). Rac2 regulates neutrophil chemotaxis, superoxide production, and myeloid colony formation through multiple distinct effector pathways. J. Immunol. 174, 4613–4620. [PubMed: 15814684]

Chapple RH, Tseng YJ, Hu T, Kitano A, Takeichi M, Hoegenauer KA, and Nakada D (2018). Lineage tracing of murine adult hematopoietic stem cells reveals active contribution to steady-state hematopoiesis. Blood Adv. 2, 1220–1228. [PubMed: 29848758]

Chen MJ, Li Y, De Obaldia ME, Yang Q, Yzaguirre AD, Yamada-Inagawa T, Vink CS, Bhandoola A, Dzierzak E, and Speck NA (2011). Erythroid/myeloid progenitors and hematopoietic stem cells originate from distinct populations of endothelial cells. Cell Stem Cell 9, 541–552. [PubMed: 22136929]

Curado S, Anderson RM, Jungblut B, Mumm J, Schroeter E, and Stainier DYR (2007). Conditional targeted cell ablation in zebrafish: a new tool for regeneration studies. Dev. Dyn. 236, 1025–1035. [PubMed: 17326133]

Curado S, Stainier DY, and Anderson RM (2008). Nitroreductase-mediated cell/tissue ablation in zebrafish: a spatially and temporally controlled ablation method with applications in developmental and regeneration studies. Nat. Protoc. 3, 948–954. [PubMed: 18536643]

Davidson AJ, and Zon LI (2004). The 'definitive' (and 'primitive') guide to zebrafish hematopoiesis. Oncogene 23, 7233–7246. [PubMed: 15378083]

Ema H, and Nakauchi H (2000). Expansion of hematopoietic stem cells in the developing liver of a mouse embryo. Blood 95, 2284–2288. [PubMed: 10733497]

Espín-Palazón R, Stachura DL, Campbell CA, García-Moreno D, Del Cid N, Kim AD, Candel S, Meseguer J, Mulero V, and Traver D (2014). Proinflammatory signaling regulates hematopoietic stem cell emergence. Cell 159, 1070–1085. [PubMed: 25416946]

Fraint E, Ulloa BA, Feliz Norberto M, Potts KS, and Bowman TV (2021). Advances in preclinical hematopoietic stem cell models and possible implications for improving therapeutic transplantation. Stem Cells Transl. Med. 10, 337–345. [PubMed: 33058566]

Galloway JL, Wingert RA, Thisse C, Thisse B, and Zon LI (2005). Loss of gata1 but not gata2 converts erythropoiesis to myelopoiesis in zebrafish embryos. Dev. Cell 8, 109–116. [PubMed: 15621534]

Godin I, and Cumano A (2002). The hare and the tortoise: an embryonic haematopoietic race. Nat. Rev. Immunol. 2, 593–604. [PubMed: 12154378]

Gutiérrez L, Caballero N, Fernández-Calleja L, Karkoulia E, and Strouboulis J (2020). Regulation of GATA1 levels in erythropoiesis. IUBMB Life 72, 89–105. [PubMed: 31769197]

Hadland B, and Yoshimoto M (2018). Many layers of embryonic hematopoiesis: new insights into B-cell ontogeny and the origin of hematopoietic stem cells. Exp. Hematol. 60, 1–9. [PubMed: 29287940]

Haghverdi L, Lun ATL, Morgan MD, and Marioni JC (2018). Batch effects in single-cell RNA-sequencing data are corrected by matching mutual nearest neighbors. Nat. Biotechnol. 36, 421–427. [PubMed: 29608177]

Hall C, Flores MV, Storm T, Crosier K, and Crosier P (2007). The zebrafish lysozyme C promoter drives myeloid-specific expression in transgenic fish. BMC Dev. Biol. 7, 42. [PubMed: 17477879]

Hao Y, Hao S, Andersen-Nissen E, Mauck WM, Zheng S, Butler A, Lee MJ, Wilk AJ, Darby C, Zagar M, et al. (2020). Integrated analysis of multimodal single-cell data. bioRxiv, 2020.10.12.335331.

Harrold I, Carbonneau S, Moore BM, Nguyen G, Anderson NM, Saini AS, Kanki JP, Jette CA, and Feng H (2016). Efficient transgenesis mediated by pigmentation rescue in zebrafish. Biotechniques 60, 13–20. [PubMed: 26757807]

He S, Tian Y, Feng S, Wu Y, Shen X, Chen K, He Y, Sun Q, Li X, Xu J, et al. (2020a). In vivo single-cell lineage tracing in zebrafish using high-resolution infrared laser-mediated gene induction microscopy. eLife 9, e52024. [PubMed: 31904340]

He S, Xu J, Qu JY, and Wen Z (2020b). Lightening the way of hematopoiesis: Infrared laser-mediated lineage tracing with high spatial-temporal resolution. Exp. Hematol. 85, 3–7. [PubMed: 32437907]

Henninger J, Santoso B, Hans S, Durand E, Moore J, Mosimann C, Brand M, Traver D, and Zon L (2017). Clonal fate mapping quantifies the number of haematopoietic stem cells that arise during development. Nat. Cell Biol. 19, 17–27. [PubMed: 27870830]

Herbomel P, Thisse B, and Thisse C (1999). Ontogeny and behaviour of early macrophages in the zebrafish embryo. Development 126, 3735–3745. [PubMed: 10433904]

Höfer T, Busch K, Klapproth K, and Rodewald HR (2016). Fate Mapping and Quantitation of Hematopoiesis In Vivo. Annu. Rev. Immunol. 34, 449–478. [PubMed: 27168243]

Hou S, Li Z, Zheng X, Gao Y, Dong J, Ni Y, Wang X, Li Y, Ding X, Chang Z, et al. (2020). Embryonic endothelial evolution towards first hematopoietic stem cells revealed by single-cell transcriptomic and functional analyses. Cell Res. 30, 376–392. [PubMed: 32203131]

Huang Y, Lu Y, He Y, Feng Z, Zhan Y, Huang X, Liu Q, Zhang J, Li H, Huang H, et al. (2019). Ikzf1 regulates embryonic T lymphopoiesis via Ccr9 and Irf4 in zebrafish. J. Biol. Chem. 294, 16152–16163. [PubMed: 31511326]

Iturri L, Freyer L, Biton A, Dardenne P, Lallemand Y, and Gomez Perdiguero E (2021). Megakaryocyte production is sustained by direct differentiation from erythromyeloid progenitors in the yolk sac until midgestation. Immunity 54, 1433–1446.e5. [PubMed: 34062116]

Kasper DM, Hintzen J, Wu Y, Ghersi JJ, Mandl HK, Salinas KE, Armero W, He Z, Sheng Y, Xie Y, et al. (2020). The N-glycome regulates the endothelial-to-hematopoietic transition. Science 370, 1186–1191. [PubMed: 33273096]

Khandekar G, Kim S, and Jagadeeswaran P (2012). Zebrafish thrombocytes: functions and origins. Adv. Hematol. 2012, 857058. [PubMed: 22778746]

Kissa K, and Herbomel P (2010). Blood stem cells emerge from aortic endothelium by a novel type of cell transition. Nature 464, 112–115. [PubMed: 20154732]

Kobayashi I, Kondo M, Yamamori S, Kobayashi-Sun J, Taniguchi M, Kanemaru K, Katakura F, and Traver D (2019). Enrichment of hematopoietic stem/progenitor cells in the zebrafish kidney. Sci. Rep. 9, 14205. [PubMed: 31578390]

Kwan KM, Fujimoto E, Grabher C, Mangum BD, Hardy ME, Campbell DS, Parant JM, Yost HJ, Kanki JP, and Chien C-B (2007). The Tol2kit: a multisite gateway-based construction kit for Tol2 transposon transgenesis constructs. Dev. Dyn. 236, 3088–3099. [PubMed: 17937395]

La Manno G, Soldatov R, Zeisel A, Braun E, Hochgerner H, Petukhov V, Lidschreiber K, Kastriti ME, Lönnerberg P, Furlan A, et al. (2018). RNA velocity of single cells. Nature 560, 494–498. [PubMed: 30089906]

Langenau DM, Ferrando AA, Traver D, Kutok JL, Hezel JP, Kanki JP, Zon LI, Look AT, and Trede NS (2004). In vivo tracking of T cell development, ablation, and engraftment in transgenic zebrafish. Proc. Natl. Acad. Sci. USA 101, 7369–7374. [PubMed: 15123839]

Lawrence C (2011). Advances in Zebrafish Husbandry and Management. In Methods in Cell Biology, Chapter 23, Detrich HW, Westerfield M, and Zon LI, eds. (Academic Press), pp. 429–451.

Le Guyader D, Redd MJ, Colucci-Guyon E, Murayama E, Kissa K, Briolat V, Mordelet E, Zapata A, Shinomiya H, and Herbomel P (2008). Origins and unconventional behavior of neutrophils in developing zebrafish. Blood 111, 132–141. [PubMed: 17875807]

Li L, Jin H, Xu J, Shi Y, and Wen Z (2011). Irf8 regulates macrophage versus neutrophil fate during zebrafish primitive myelopoiesis. Blood 117, 1359–1369. [PubMed: 21079149]

Li L, Yan B, Shi Y-Q, Zhang W-Q, and Wen Z-L (2012). Live imaging reveals differing roles of macrophages and neutrophils during zebrafish tail fin regeneration. J. Biol. Chem. 287, 25353–25360. [PubMed: 22573321]

Lin HF, Traver D, Zhu H, Dooley K, Paw BH, Zon LI, and Handin RI (2005). Analysis of thrombocyte development in CD41-GFP transgenic zebrafish. Blood 106, 3803–3810. [PubMed: 16099879]

Long Q, Meng A, Wang H, Jessen JR, Farrell MJ, and Lin S (1997). GATA-1 expression pattern can be recapitulated in living transgenic zebrafish using GFP reporter gene. Development 124, 4105–4111. [PubMed: 9374406]

McGrath KE, Frame JM, Fegan KH, Bowen JR, Conway SJ, Catherman SC, Kingsley PD, Koniski AD, and Palis J (2015). Distinct Sources of Hematopoietic Progenitors Emerge before HSCs and Provide Functional Blood Cells in the Mammalian Embryo. Cell Rep. 11, 1892–1904. [PubMed: 26095363]

McInnes L, Healy J, and Melville J (2018). UMAP: Uniform Manifold Approximation and Projection for dimension reduction. Preprint at. https://arxiv.org/abs/1802.03426.

Medvinsky A, and Dzierzak E (1996). Definitive hematopoiesis is autonomously initiated by the AGM region. Cell 86, 897–906. [PubMed: 8808625]

Mesquita A, Pereira J, and Jenny A (2020). Streamlined particle quantification (SParQ) plug-in is an automated fluorescent vesicle quantification plug-in for particle quantification in Fiji/ImageJ. Autophagy 16, 1711–1717. [PubMed: 31752589]

Mosimann C, Kaufman CK, Li P, Pugach EK, Tamplin OJ, and Zon LI (2011). Ubiquitous transgene expression and Cre-based recombination driven by the ubiquitin promoter in zebrafish. Development 138, 169–177. [PubMed: 21138979]

Mosimann C, Panáková D, Werdich AA, Musso G, Burger A, Lawson KL, Carr LA, Nevis KR, Sabeh MK, Zhou Y, et al. (2015). Chamber identity programs drive early functional partitioning of the heart. Nat. Commun. 6, 8146. [PubMed: 26306682]

Müller AM, Medvinsky A, Strouboulis J, Grosveld F, and Dzierzak E (1994). Development of hematopoietic stem cell activity in the mouse embryo. Immunity 1, 291–301. [PubMed: 7889417]

Murayama E, Kissa K, Zapata A, Mordelet E, Briolat V, Lin HF, Handin RI, and Herbomel P (2006). Tracing hematopoietic precursor migration to successive hematopoietic organs during zebrafish development. Immunity 25, 963–975. [PubMed: 17157041]

Nottingham WT, Jarratt A, Burgess M, Speck CL, Cheng J-F, Prabhakar S, Rubin EM, Li P-S, Sloane-Stanley J, Kong-A-San J, and de Bruijn MF (2007). Runx1-mediated hematopoietic stem-cell emergence is controlled by a Gata/Ets/SCL-regulated enhancer. Blood 110, 4188–4197. [PubMed: 17823307]

Oh S-Y, Kim JY, and Park C (2015). The ETS Factor, ETV2: a Master Regulator for Vascular Endothelial Cell Development. Mol. Cells 38, 1029–1036. [PubMed: 26694034]

Patterson LJ, Gering M, Eckfeldt CE, Green AR, Verfaillie CM, Ekker SC, and Patient R (2007). The transcription factors Scl and Lmo2 act together during development of the hemangioblast in zebrafish. Blood 109, 2389–2398. [PubMed: 17090656]

Prummel KD, Hess C, Nieuwenhuize S, Parker HJ, Rogers KW, Kozmikova I, Racioppi C, Brombacher EC, Czarkwiani A, Knapp D, et al. (2019). A conserved regulatory program initiates lateral plate mesoderm emergence across chordates. Nat. Commun. 10, 3857. [PubMed: 31451684]

Renaud O, Herbomel P, and Kissa K (2011). Studying cell behavior in whole zebrafish embryos by confocal live imaging: application to hematopoietic stem cells. Nat. Protoc. 6, 1897–1904. [PubMed: 22082984]

Renshaw SA, Loynes CA, Trushell DM, Elworthy S, Ingham PW, and Whyte MK (2006). A transgenic zebrafish model of neutrophilic inflammation. Blood 108, 3976–3978. [PubMed: 16926288]

Robertson AL, Avagyan S, Gansner JM, and Zon LI (2016). Understanding the regulation of vertebrate hematopoiesis and blood disorders - big lessons from a small fish. FEBS Lett. 590, 4016–4033. [PubMed: 27616157]

Rojo R, Raper A, Ozdemir DD, Lefevre L, Grabert K, Wollscheid-Lengeling E, Bradford B, Caruso M, Gazova I, Sánchez A, et al. (2019). Deletion of a Csf1r enhancer selectively impacts CSF1R expression and development of tissue macrophage populations. Nat. Commun. 10, 3215. [PubMed: 31324781]

Sánchez-Iranzo H, Galardi-Castilla M, Minguillón C, Sanz-Morejón A, González-Rosa JM, Felker A, Ernst A, Guzmán-Martínez G, Mosimann C, and Mercader N (2018). Tbx5a lineage tracing shows cardiomyocyte plasticity during zebrafish heart regeneration. Nat. Commun. 9, 428. [PubMed: 29382818]

Sauteur L, Krudewig A, Herwig L, Ehrenfeuchter N, Lenard A, Affolter M, and Belting H-G (2014). Cdh5/VE-cadherin promotes endothelial cell interface elongation via cortical actin polymerization during angiogenic sprouting. Cell Rep. 9, 504–513. [PubMed: 25373898]

Schindelin J, Arganda-Carreras I, Frise E, Kaynig V, Longair M, Pietzsch T, Preibisch S, Rueden C, Saalfeld S, Schmid B, et al. (2012). Fiji: an open-source platform for biological-image analysis. Nat. Methods 9, 676–682. [PubMed: 22743772]

Shafizadeh E, Peterson RT, and Lin S (2004). Induction of reversible hemolytic anemia in living zebrafish using a novel small molecule. Comp. Biochem. Physiol. C Toxicol. Pharmacol 138, 245–249. [PubMed: 15533782]

Soares-da-Silva F, Freyer L, Elsaid R, Burlen-Defranoux O, Iturri L, Sismeiro O, Pinto-do-Ó P, Gomez-Perdiguero E, and Cumano A (2021). Yolk sac, but not hematopoietic stem cell-derived progenitors, sustain erythropoiesis throughout murine embryonic life. J. Exp. Med. 218, e20201729. [PubMed: 33566111]

Song H-D, Sun X-J, Deng M, Zhang G-W, Zhou Y, Wu X-Y, Sheng Y, Chen Y, Ruan Z, Jiang C-L, et al. (2004). Hematopoietic gene expression profile in zebrafish kidney marrow. Proc. Natl. Acad. Sci. USA 101, 16240–16245. [PubMed: 15520368]

Soza-Ried C, Hess I, Netuschil N, Schorpp M, and Boehm T (2010). Essential role of c-myb in definitive hematopoiesis is evolutionarily conserved. Proc. Natl. Acad. Sci. USA 107, 17304–17308. [PubMed: 20823231]

Stachura DL, and Traver D (2016). Cellular dissection of zebrafish hematopoiesis. Methods Cell Biol. 133, 11–53. [PubMed: 27263407]

Suster ML, Kikuta H, Urasaki A, Asakawa K, and Kawakami K (2009). Transgenesis in zebrafish with the tol2 transposon system. Methods Mol. Biol. 561, 41–63. [PubMed: 19504063]

Tamplin OJ, Durand EM, Carr LA, Childs SJ, Hagedorn EJ, Li P, Yzaguirre AD, Speck NA, and Zon LI (2015). Hematopoietic stem cell arrival triggers dynamic remodeling of the perivascular niche. Cell 160, 241–252. [PubMed: 25594182]

Tian Y, Xu J, Feng S, He S, Zhao S, Zhu L, Jin W, Dai Y, Luo L, Qu JY, and Wen Z (2017). The first wave of T lymphopoiesis in zebrafish arises from aorta endothelium independent of hematopoietic stem cells. J. Exp. Med. 214, 3347–3360. [PubMed: 28931624]

Trapnell C, Cacchiarelli D, Grimsby J, Pokharel P, Li S, Morse M, Lennon NJ, Livak KJ, Mikkelsen TS, and Rinn JL (2014). The dynamics and regulators of cell fate decisions are revealed by pseudotemporal ordering of single cells. Nat. Biotechnol. 32, 381–386. [PubMed: 24658644]

Traver D, Paw BH, Poss KD, Penberthy WT, Lin S, and Zon LI (2003). Transplantation and in vivo imaging of multilineage engraftment in zebrafish bloodless mutants. Nat. Immunol. 4, 1238–1246. [PubMed: 14608381]

Trede NS, and Zon LI (1998). Development of T-cells during fish embryogenesis. Dev. Comp. Immunol. 22, 253–263. [PubMed: 9700456]

Vink CS, Calero-Nieto FJ, Wang X, Maglitto A, Mariani SA, Jawaid W, Göttgens B, and Dzierzak E (2020). Iterative Single-Cell Analyses Define the Transcriptome of the First Functional Hematopoietic Stem Cells. Cell Rep. 31, 107627. [PubMed: 32402290]

Waas B, and Maillard I (2017). Fetal hematopoietic stem cells are making waves. Stem Cell Investig. 4, 25.

Wang H, Liu C, Liu X, Wang M, Wu D, Gao J, Su P, Nakahata T, Zhou W, Xu Y, et al. (2018). MEIS1 Regulates Hemogenic Endothelial Generation, Megakaryopoiesis, and Thrombopoiesis in Human Pluripotent Stem Cells by Targeting TAL1 and FLI1. Stem Cell Reports 10, 447–460. [PubMed: 29358086]

Willett CE, Kawasaki H, Amemiya CT, Lin S, and Steiner LA (2001). Ikaros expression as a marker for lymphoid progenitors during zebrafish development. Dev. Dyn. 222, 694–698. [PubMed: 11748838]

Xue Y, Liu D, Cui G, Ding Y, Ai D, Gao S, Zhang Y, Suo S, Wang X, Lv P, et al. (2019). A 3D Atlas of Hematopoietic Stem and Progenitor Cell Expansion by Multi-dimensional RNA-Seq Analysis. Cell Rep. 27, 1567–1578.e5. [PubMed: 31042481]

Zakrzewska A, Cui C, Stockhammer OW, Benard EL, Spaink HP, and Meijer AH (2010). Macrophage-specific gene functions in Spi1-directed innate immunity. Blood 116, e1–e11. [PubMed: 20424185]

Zhan Y, Huang Y, Chen J, Cao Z, He J, Zhang J, Huang H, Ruan H, Luo L, and Li L (2018). The caudal dorsal artery generates hematopoietic stem and progenitor cells via the endothelial-to-hematopoietic transition in zebrafish. J. Genet. Genomics, Published online June 8, 2018. 10.1016/j.jgg.2018.02.010.

Zhang Y, Jin H, Li L, Qin FXF, and Wen Z (2011). cMyb regulates hematopoietic stem/progenitor cell mobilization during zebrafish hematopoiesis. Blood 118, 4093–4101. [PubMed: 21856868]

Zhou F, Li X, Wang W, Zhu P, Zhou J, He W, Ding M, Xiong F, Zheng X, Li Z, et al. (2016). Tracing haematopoietic stem cell formation at single-cell resolution. Nature 533, 487–492. [PubMed: 27225119]

Zhou Y, Zhou B, Pache L, Chang M, Khodabakhshi AH, Tanaseichuk O, Benner C, and Chanda SK (2019). Metascape provides a biologist-oriented resource for the analysis of systems-level datasets. Nat. Commun. 10, 1523. [PubMed: 30944313]

Zhu Q, Gao P, Tober J, Bennett L, Chen C, Uzun Y, Li Y, Howell ED, Mumau M, Yu W, et al. (2020). Developmental trajectory of prehematopoietic stem cell formation from endothelium. Blood 136, 845–856. [PubMed: 32392346]

Zovein AC, Hofmann JJ, Lynch M, French WJ, Turlo KA, Yang Y, Becker MS, Zanetta L, Dejana E, Gasson JC, et al. (2008). Fate tracing reveals the endothelial origin of hematopoietic stem cells. Cell Stem Cell 3, 625–636. [PubMed: 19041779]

Highlights

- Nascent HSC and HSC-independent progenitors possess unique gene signatures
- Embryonic lymphomyelopoiesis is sustained by HSC-independent progenitors
- Nascent HSCs robustly regenerate but display differentiation latency

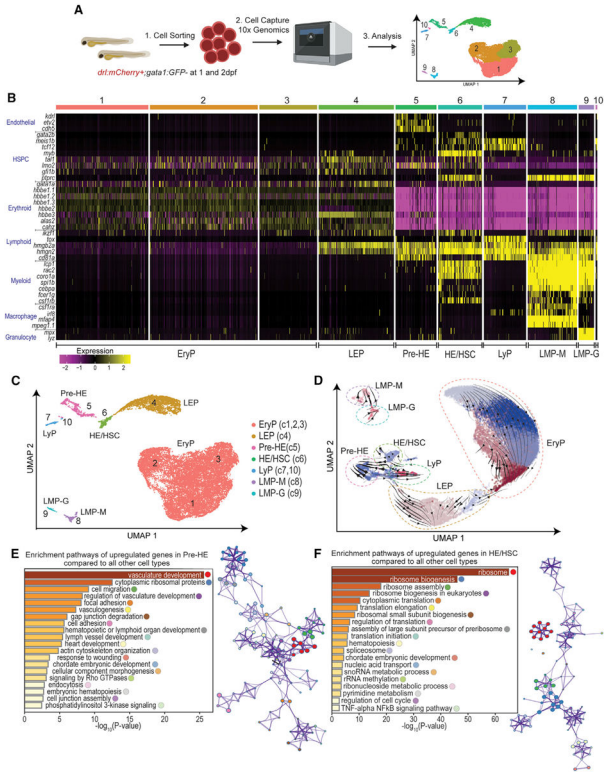

Figure 1. Developmental hematopoietic heterogeneity identified in zebrafish with single-cell RNA sequencing (scRNA-seq)

(A) Schema of scRNA-seq experiment: (1) *drl:mCherry*$^{+}$;*gata1:GFP*$^{-}$ cells were isolated by fluorescence-activated cell sorting (FACS) from pools of 1 and 2 dpf embryos to enrich for HSPCs, (2) 10X Genomics single-cell RNA libraries were prepared and sequenced, and (3) downstream computational analysis showing that UMAP dimensional reduction and unsupervised clustering of *drl:mCherry*$^{+}$;*gata1:GFP*$^{-}$ cells at 1 and 2 dpf with Monocle3 gives 10 clusters.

(B) Cell-type identification of the 10 Monocle3 clusters performed using key hematopoietic marker genes supported by previous zebrafish, murine, and human literature. Cell types identified include erythroid progenitors (EryPs), clusters 1–3 (c1–c3); lympho-erythroid-primed progenitor (LEP), cluster 4 (c4); pre-hemogenic endothelial cells (pre-HE), cluster 5 (c5); hemogenic endothelial cells generating HSCs (HE/HSC), cluster 6 (c6); lymphoid progenitor (LyP), cluster 7 and 10 (c7,10); lymphomyeloid progenitor with higher macrophage marker expression (LMP-M), cluster 8 (c8); and lymphomyeloid progenitor with higher granulocyte marker expression (LMP-G), cluster 9 (c9). Expression bar: scaling is performed per gene where mean is close to 0 and standard deviation of 1. Only genes with the highest scaled expression value will show the brightest yellow color in any of the cells (standard deviation above −2), and those that have the lowest scaled expression will be purple (standard deviation below 2).

(C) The cell-type classifications in UMAP space as identified in (B).

(D) RNA velocities overlaid over UMAP clusters of *drl:mCherry*$^{+}$*gata1:GFP*$^{-}$ cells at 1 and 2 dpf. The different colors represent the Seurat clusters derived from reprocessing the data. The dotted lines encircling each cluster are cell types identified with previously used marker

genes (refer to Figure S1D). Arrows indicate inferred differentiation trajectory as determined by RNA velocities.

(E and F) Enrichment pathway analysis of upregulated top marker genes in pre-HE (E) and HE/HSC (F) clusters, conducted using Metascape. Top 200 markers selected using Monocle3 with the following criteria: fraction expressing >10% and marker test $p < 0.00005$. The colored circles after each term in the significance bar plot (left) represent a colored dot on the network representation (right).

See also Figure S1.

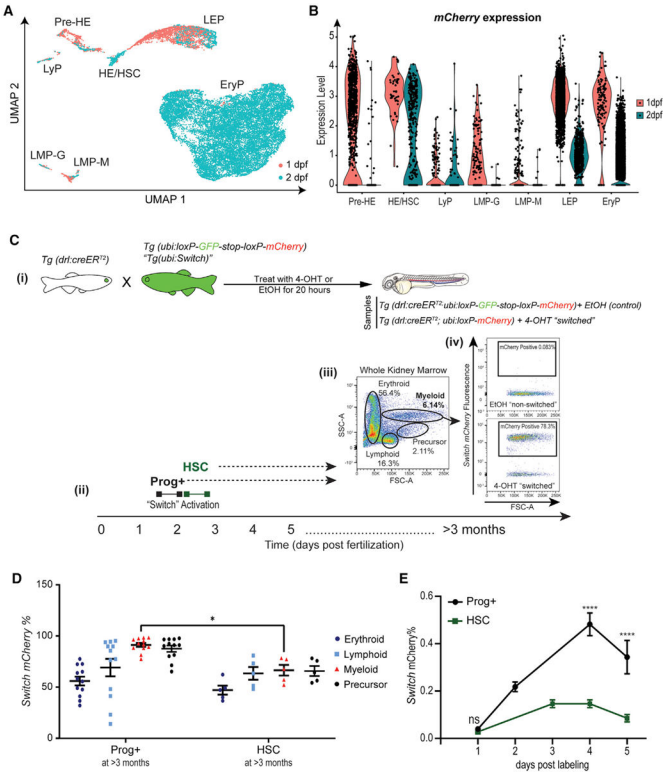

Figure 2. Dynamic regulation of the *drl* promoter distinguishes HSPC subsets

(A) UMAP dimensional reduction and unsupervised clustering of *drl:mCherry*$^{+}$;*gata1:GFP*$^{-}$ cells at 1 and 2 dpf showing their original collection time point.

(B) mCherry expression level driven by the *drl* promoter for the different cell types collected at 1 and 2 dpf.

(C) (i) Schematic illustrating *drl*-specific, 4-OHT-inducible lineage-tracing system. *Tg(drl:creER^{T2})* homozygous transgenic fish were crossed with *hemizygous ubi:loxP-GFP-stop-loxP-mCherry* (*ubi:Switch*). (ii) Zebrafish embryos were exposed to 12 μM 4-OH-tamoxifen (4-OHT) or ethanol (EtOH) vehicle control for 20 h starting at either 30 hpf (labeled as Prog+, which includes embryonic progenitors and HSCs) or 54 hpf (labeled as HSC). Those embryos exposed to 4-OHT induce Cre recombination of *loxP* sites, leading to a permanent "switch" excising the *GFP* cassette and resulting in expression of mCherry fluorescence. The resulting mCherry^{+} cells are the descendants of Prog+− and HSC-labeled cells. (iii) Representative flow cytometry analysis: forward (FSC) and side scatter (SSC) parameters were used to define the major blood cell populations (erythroid, myeloid, lymphoid, and precursor) in whole kidney marrow (WKM) (>3 months). (iv) The frequency of mCherry^{+} cells within each cell lineage was then calculated. Example flow cytometry plots (right) of mCherry contribution to the myeloid population. Gates were set based on EtOH-treated "non-switched" controls.

(D) Quantification of mCherry^{+} percentage from experimental groups Prog+ and HSCs within each blood cell lineage found in WKM at >3 months post-fertilization (zebrafish adulthood). Data points represent individual zebrafish WKM with mean ± SEM (n = 5–12).

(E) Quantification of mCherry^{+} percentage at 1–5 days post-labeling in Prog+ and HSC-labeled cohorts. n = 5–11 samples, 7–10 pooled larvae per sample. Two-way ANOVA with

Sidak's multiple comparison test was used for analysis (mean ± SEM). *$p < 0.05$; ****$p \leq 0.0001$. See also Figure S2.

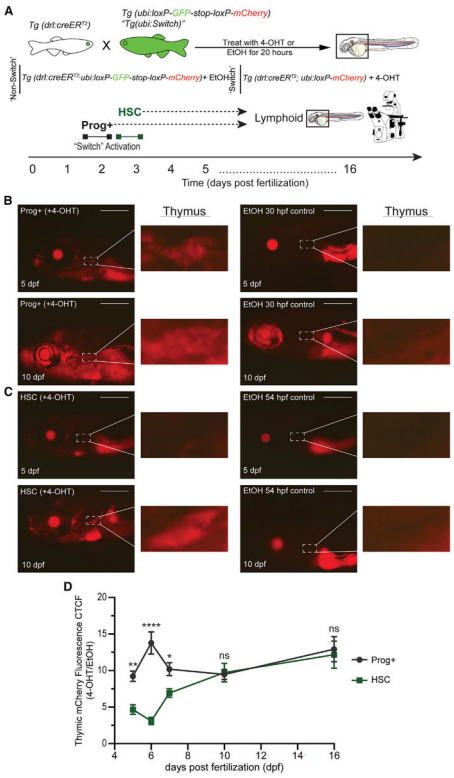

Figure 3. Thymic T cell contribution by embryonic progenitors and HSCs is distinct

(A) Experimental schema of 4-OHT-inducible lineage tracing to examine larval T cell production in the thymus from Prog+− and HSC-labeled cohorts.

(B and C) Fluorescent images of 4-OHT-induced switch (left) and EtOH non-switched controls (right) *Tg(drl:creER^{T2};ubi:Switch)* larvae for Prog+ (B) and HSC (C) populations. Top images are 5 dpf larvae, and bottom images are 10 dpf larvae. Dashed box and inset showing the thymus where T cells colonize. mCherry^{+} fluorescence corresponds to *drl*+ switched daughter cells. Scale bars, 500 μm. Representative images are shown, with quantification in (D).

(D) Quantification of mCherry fluorescence intensity in the thymic region in larvae of Prog+ − and HSC-labeled cohorts measured over a time course of 5–16 dpf. Mean ± SEM of the mCherry^{+} corrected total cell fluorescence (CTCF) at each time point is shown. Two-way ANOVA with Sidak's multiple comparison (n = 6–30 per larvae/day). *p ≤ 0.05; **p ≤ 0.01; ****p ≤ 0.0001. See also Figure S3.

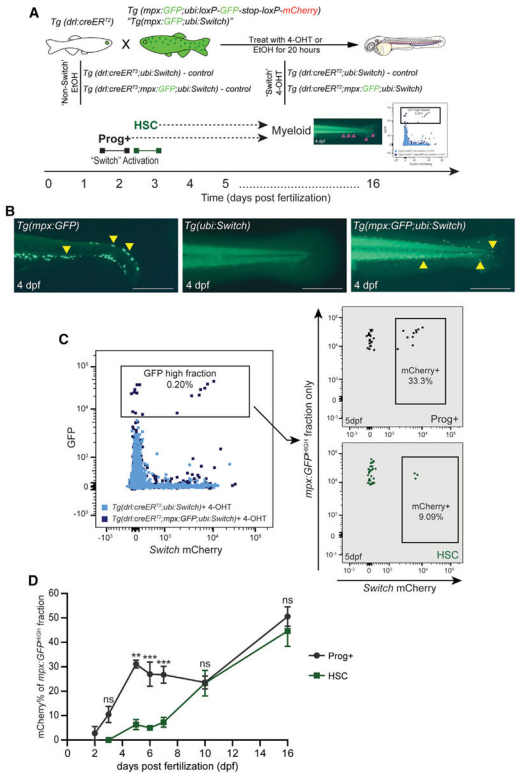

Figure 4. Granulocyte contribution by embryonic progenitors and HSCs is distinct

(A) Experimental schema of 4-OHT-inducible lineage tracing to examine larval granulocyte production from Prog+− and HSC-labeled cohorts. Granulocytes are distinguished by high GFP expression from the *mpx:GFP* transgene compared to the low GFP intensity of *ubi:Switch*.

(B) Fluorescent images of the tail region of 4 dpf *Tg(mpx:GFP)* (left), *Tg(ubi:Switch)* (middle), and *Tg(mpx:GFP;ubi:Switch)* (right). *mpx:GFP*$^{+}$ granulocytes are denoted by yellow arrowheads. Scale bars, 500 μm.

(C) Overlay flow cytometry plot (left) showing higher levels of *mpx:GFP* signal in *Tg(drl:reER*^{T2}*;mpx:GFP;ubi:Switch)* (dark purple) compared to *Tg(drl:creER*^{T2}*;ubi:Switch)* control (light blue). The frequency of mCherry^{+} switch cells was then calculated in the GFP^{high} fraction in Prog+− and HSC-labeled cohorts. Representative flow cytometry plots from 5 dpf larvae (right).

(D) Quantification of percentage of mCherry^{+} cells within the *mpx:GFP*^{high} fraction in Prog+ and HSC populations measured over a time course of 2–16 dpf (n = 3–7 samples, 7–10 fish per sample). Mean ± SEM of the mCherry^{+} percentage at each time point is shown. Two-way ANOVA with Sidak's multiple comparison was used for this analysis. **p ≤ 0.01; ***p ≤ 0.001. See also Figure S4.

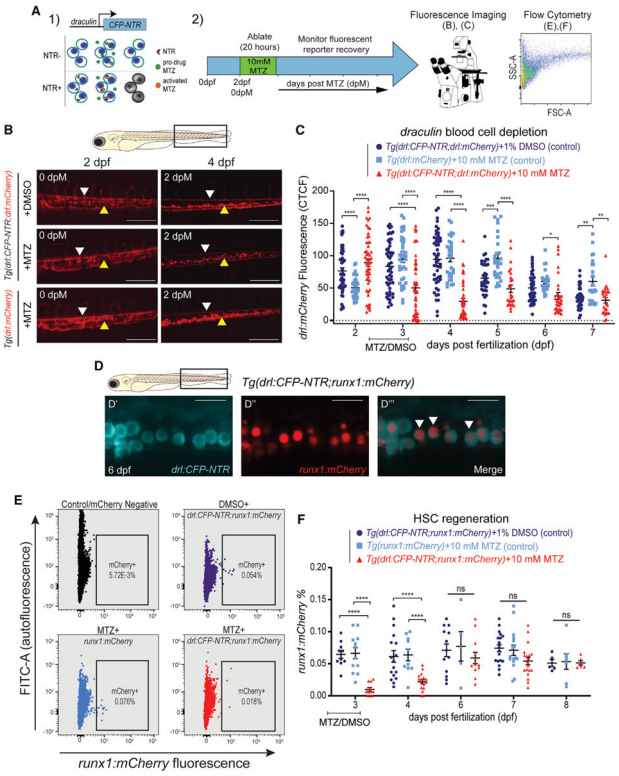

Figure 5. HSCs regenerate following their targeted depletion in early development

(A) Experimental schema of regeneration assay: (1) mechanism: *drl* promoter drives expression of a *CFP-NTR* (nitroreductase) transgene. NTR converts metronidazole (MTZ) into a toxic intermediate that triggers apoptosis of only *drl:CFP-NTR*-expressing cells; (2) timeline: *Tg(drl:CFP-NTR)* or control larvae were treated with 10 mM MTZ or 1% DMSO vehicle control for 20 h from 54–74 h post-fertilization (~2–3 dpf) to specifically target HSCs and were then monitored for their recovery using fluorescence imaging and flow cytometry.

(B) Fluorescent images of *Tg(drl:CFP-NTR*$^{+}$*;drl:mCherry*$^{+}$*)* and *Tg(drl:mCherry*$^{+}$*)* embryos treated with 10 mM MTZ or 1% DMSO (control) at 2 and 4 dpf (0 and 2 days post-MTZ [dpM], respectively). Arrowheads indicate remaining stationary (yellow) and circulatory (white) cells within the caudal hematopoietic tissue (CHT; boxed region in schematic of zebrafish larva, above). Scale bars, 500 μm.

(C) Quantification of *drl:mCherry* CTCF levels in treated groups and control groups: (*Tg(drl:CFP-NTR;drl:mCherry)* + 1% DMSO (purple), *Tg(drl:mCherry)* + 10 mM MTZ (light blue); and *Tg(drl:CFP-NTR;drl:mCherry)* + 10 mM MTZ (red) (n = 17–54 larvae).

(D) Confocal fluorescent images showing cytoplasmic *drl:CFP-NTR* expression (D′), nuclear *runx1:mCherry* expression (marking HSPCs) (D′′), and merged (D′′′) within the CHT of a 6 dpf zebrafish, with white arrowheads indicating double-positive cells. Scale bars, 500 μm.

(E) Flow cytometry plots of *runx1:mCherry* and fluorescein isothiocyanate (FITC) (autofluorescence control) in untreated negative controls (black), *Tg(drl:CFP-NTR;runx1:mCherry)* + 1% DMSO, *Tg(runx1:mCherry)* + 10 mM MTZ; and *Tg(drl:CFP-NTR;runx1:mCherry)* + 10 mM MTZ.

(F) Quantification of *runx1:mCherry*$^{+}$ % from (E) flow cytometry experiments in treated and control groups. n = 5–19, 7–10 pooled larvae per sample. Two-way ANOVA with Tukey's multiple comparisons test was used for all statistical analyses. Plots are individual points for each biological replicate with mean ± SEM. ****$p \leq 0.0001$. See also Figure S5.

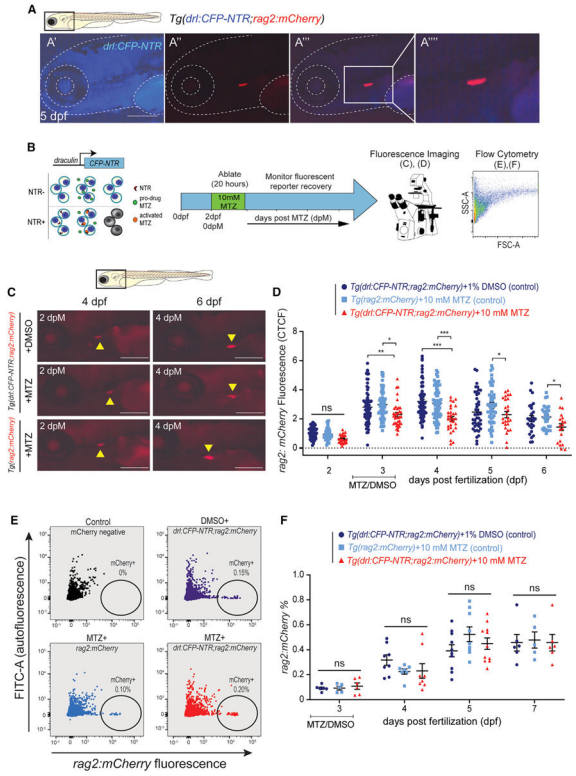

Figure 6. Depletion of HSCs has a negligible impact on T cell seeding of larval thymus

(A) Fluorescent images of *drl:CFP-NTR* (A′), rag2:mCherry (marking T-lymphocytes) (A′′) and merged (A′′′) at 5 dpf in the thymic lymphoid tissue. Scale bars, 500 μm. Merged fluorescent image (A′′′′) shows higher magnification image of (A′′′).

(B) Experimental schema of the NTR/MTZ system.

(C) Fluorescent images of *Tg(drl:CFP-NTR^{+}; rag2:mCherry^{+})* and *Tg(rag2:mCherry^{+})* larvae shown at 4 and 6 dpf (2 and 4 dpM, respectively) after depletion of HSCs using the NTR/MTZ system. Yellow arrowheads indicate *rag2:mCherry^{+}* fluorescent lymphocytes within the thymus. Scale bars, 500 μm.

(D) Quantification of *rag2:mCherry* fluorescence CTCF levels in *Tg(drl:CFP-NTR^{+};rag2:mCherry^{+})* and *Tg(rag2:mCherry^{+})* zebrafish treated with 10 mM MTZ or 1% DMSO (n = 19–72 larvae).

(E) Flow cytometry plots of *rag2:mCherry* and FITC (autofluorescence control) in untreated negative controls (black); *Tg(drl:CFP-NTR;rag2:mCherry)* + 1% DMSO (purple); *Tg(rag2:mCherry)* + 10 mM MTZ (light blue); and *Tg(drl:CFP-NTR;rag2:mCherry)* + 10 mM MTZ (red).

(F) Quantification of *rag2:mCherry*% from (E) flow cytometry experiments in treated and control groups; n = 4–11, 7–10 pooled larvae per sample.

Two-way ANOVA with Tukey's multiple comparisons test was used for all statistical analyses. Plots are individual data points for each biological replicate with mean ± SEM. ns, not significant; *p < 0.05; **p ≤ 0.01; ***p ≤ 0.001.

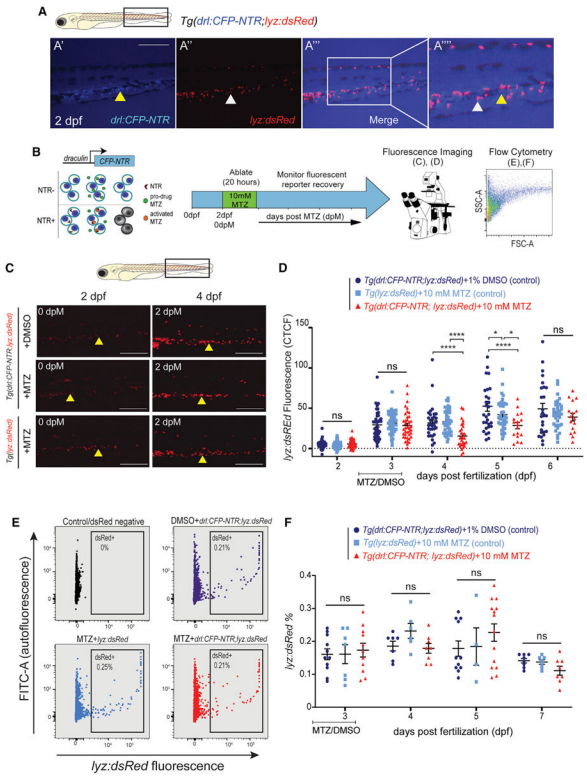

Figure 7. Depletion of HSCs has a negligible impact on granulocyte frequency

(A) Fluorescent images of *drl:CFP-NTR* (A′), *lyz:dsRed* (marking myeloid cells) (A′′), and merged (A′′′) at 2 dpf showing minimal co-expression. Scale bars, 500 μm. White arrow marks *lyz:dsRed* single-positive granulocyte, and yellow arrowhead marks *drl:CFP-NTR* single-positive cell; 1.75× inset in (A′′′′).

(B) Experimental schema of the NTR/MTZ system.

(C) Fluorescent images of *Tg(drl:CFP-NTR^{+};lyz:dsRed^{+})* and *Tg(lyz:dsRed^{+})* embryos treated with either 1% DMSO or 10 mM MTZ, shown at 2 and 4 dpf (0 and 2 dpM, respectively). Yellow arrowhead showing stationary cells in the CHT region. Scale bars, 500 μm.

(D) Quantification of *lyz:dsRed* fluorescence CTCF levels in *Tg(drl:CFP-NTR^{+};lyz:dsRed^{+})* and *Tg(lyz:dsRed+)* embryos treated with 10 mM MTZ or 1% DMSO (n = 16–45).

(E) Flow cytometry plots *of lyz:dsRed* and FITC (autofluorescence control) in untreated negative controls (black); *Tg(drl:CFP-NTR;lyz:dsRed*) + 1% DMSO (purple); *Tg(lyz:dsRed)* + 10 mM MTZ (light blue); and *Tg(drl:CFP-NTR;lyz:dsRed)* + 10 mM MTZ (red).

(F) Quantification of *lyz:dsRed*% from flow cytometry experiments (E) in treated and control groups (n = 4–14 samples, 7–10 pooled larvae per sample).

Two-way ANOVA with Tukey's multiple comparisons test was used for all statistical analyses. Plots are individual data points for each biological replicate with mean ± SEM. ns, not significant; *p < 0.05; ****p ≤ 0.0001.

KEY RESOURCES TABLE

REAGENT or RESOURCE	SOURCE	IDENTIFIER
Chemicals, peptides, and recombinant proteins		
Metronidazole	Sigma	M3761
Dimethyl sulfoxide (DMSO)	Sigma	D5879
(Z)-4-Hydroxytamoxifen	Sigma	H7904
4'6-Diamidino-2-phenlyindole (DAPI)	Sigma	D8417
Experimental models: Organisms/strains		
Zebrafish *Tg(drl:mCherry)*	Sánchez-Iranzo et al., 2018	ZDB-TGCONSTRCT-171031–8
Zebrafish *Tg(gata1:eGFP)*	Shafizadeh et al., 2004	ZDB-TGCONSTRCT-070117–153
Zebrafish *Tg(runx1+23:nls-mCherry)*	Tamplin et al., 2015	ZDB-TGCONSTRCT-150512–2
Zebrafish *Tg(mpx:GFP)*	Renshaw et al., 2006	ZDB-TGCONSTRCT-070118–1
Zebrafish *Tg(drl:CreER^{T2})*	Mosimann et al., 2015	ZDB-TGCONSTRCT-160129–2
Zebrafish *Tg(ubi:loxP-GFP-loxP-stop-mCherry)*	Mosimann et al., 2011	ZDB-TGCONSTRCT-110124–1
Zebrafish *Tg(drl:CFP:NTR)*	This paper	NA
Zebrafish *Tg(cd41:eGFP)*	Lin et al., 2005	ZDB-TGCONSTRCT-070117–128
Zebrafish *Tg(rag2:mCherry)*	Harrold et al., 2016	ZDB-TGCONSTRCT-160329–2
Zebrafish *Tg(lyz:dsRed)*	Hall et al., 2007	ZDB-TGCONSTRCT-071109–3
Software and algorithms		
Single cell alignment, filtering, QC	Cell Ranger v4.0.0	https://support.10xgenomics.com/
Single cell data analysis pipeline	Seurat v4	https://satijalab.org/seurat/
Single cell data analysis pipeline and lineage construction: Pseudotime Analysis	Monocle3	https://cole-trapnell-lab.github.io/monocle3
Single cell lineage construction: RNA Velocity	velocyto	http://velocyto.org/
Single cell lineage construction: RNA Velocity	scVelo	https://scvelo.readthedocs.io/
Zebrafish Homolog Conversion	Ensembl BioMart	https://www.ensembl.org/
Gene Enrichment Network Analysis	Metascape	https://metascape.org/
Image collection	Zeiss Zen 2 software	https://www.zeiss.com/corporate/int/home.html
Image analysis	ImageJ	https://imagej.nih.gov/ij/
Image analysis	Photoshop CC 2019	https://www.adobe.com/
Image Analysis: Automatic particle quantification	SparQ	https://github.com/sparq-plugin/sparq
Image formatting	Adobe Illustrator CC 2019	https://www.adobe.com/
Flow cytometric analysis	FlowJo versions 10.6 – 10.7.1	https://www.flowjo.com/
Data analysis	GraphPad Prism version 8	https://www.graphpad.com/
Deposited data		
Single cell RNA seq	This paper	GSE182213